Investigation into the Local and Global Bifurcations of the Whirling Planar Pendulum

Griffin N. Hyde

Thesis submitted to the Faculty of the

Virginia Polytechnic Institute and State University

in partial fulfillment of the requirements for the degree of

Master of Science

in

Aerospace Engineering

Craig A. Woolsey, Chair

Steve C. Southward

Michael K. Philen

May 14, 2019

Blacksburg, Virginia

Keywords: Chaos theory, Bifurcation theory, Whirling Planar Pendulum

Investigation into the Local and Global Bifurcations of the Whirling Planar Pendulum

Griffin N. Hyde

(ABSTRACT)

This thesis details the investigation into the Whirling Planar Pendulum system. The WPP is a pendulum that is spun around a vertical spin axis at a controllable horizontal offset. This dynamical system exhibits both local and global bifurcations. The local pitchfork bifurcation leads to the splitting of a single stable equilibrium point into three (two stable and one unstable), as the spin rate is increased. The global bifurcations lead to two independent types of chaotic oscillations which are induced by sinusoidal excitations. The types of chaos are each associated with one of two homoclinic orbits in the system's phase portraits. The onset of each type of chaos is investigated through Melnikov's Method applied to the system's Hamiltonian, to find parameters at which the stable and unstable manifolds intersect transversely, indicating the onset of chaotic motion. These results are compared to simulation results, which suggest chaotic motion through the appearance of strange attractors in the Poincaré maps. Additionally, evidence of the WPP system experiencing both types of chaos simultaneously was found, resulting in a merger of two distinct types of strange attractor.

Investigation into the Local and Global Bifurcations of the Whirling Planar Pendulum

Griffin N. Hyde

(GENERAL AUDIENCE ABSTRACT)

This report details the investigation into the Whirling Planar Pendulum system. The WPP is a pendulum that is spun around a vertical spin axis at a controllable horizontal offset. This system can be used to investigate what are known as local and global bifurcations. A local bifurcation occurs when the single equilibrium state (corresponding to the pendulum hanging straight down) when spun at low speeds, bifurcates into three equilibria when the spin rate is increased beyond a certain value. The global bifurcations occur when the system experiences sinusoidal forcing near certain equilibrium conditions. The resulting chaotic oscillations are investigated using Melnikov's method, which determines when the sinusoidal forcing results in chaotic motion. This chaotic motion comes in two types, which cause the system to behave in different ways. Melnikov's method, and results from a simulation were used to determine the parameter values in which the pendulum experiences each type of chaos. It was seen that at certain parameter values, the WPP experiences both types of chaos, supporting the observation that these types of chaos are not necessarily independent of each other, but can merge and interact.

Contents

List of Figures

Chapter 1

Introduction

The Whirling Planar Pendulum (WPP) is a multi-dimensional, non-linear oscillator that can be used to investigate interesting dynamic phenomena. The Whirling Planar Pendulum consists of a pendulum that is spun at an angular spin rate ω, at an offset distance Δ from the vertical axis. The spinning motion and the offset of the spin axis affect the pendulum's angle θ. When $\Delta = 0$ at a constant value of ω, there exist equilibrium values of θ at which the pendulum rests vertically upward or downward. The downward equilibrium exhibits a local pitchfork bifurcation at a critical spin rate ω_c, where the single equilibrium value at $\theta = 0$ (directly downwards) splits into three equilibria. Two of these are stable at non-zero angles of θ, with equal magnitude but opposite sign. The third is the now unstable equilibrium at $\theta = 0$. When $\Delta = 0$, this bifurcation occurs at a critical spin rate ω_c. When $\Delta \neq 0$, the bifurcation is perturbed, and while one nonzero stable equilibrium exists at ω_c as ω is increased, the second stable equilibrium does not appear until some $\omega > \omega_c$.

By treating the square of the spin rate, ω^2, and the horizontal displacement, Δ, as parameters, the vertical component of angular momentum is conserved for a given value of ω^2, and the system can be reduced to a conservative planar Hamiltonian system. This allows it to be modeled as a single degree of freedom non-linear oscillator. This simplification allows for many tools in analyzing its dynamics, and these dynamics can be visualized in the lower-dimensional phase space.

The particular apparatus used in this report allows for independent control of both ω and

Δ, both of which can be varied throughout the experiment. The focus of this report is to investigate the phase space and homoclinic orbits corresponding to inherent chaos in the system when sinusoidal forcing is present. The WPP contains two sets of homoclinic orbits, which are periodic orbits that join a saddle point to itself. These orbits are the intersections of stable and unstable manifolds, and lead to global homoclinic bifurcations, and thus, the possibility of chaotic motion. Evidence of chaos is examined in the Poincaré map in the form of a strange attractor. Occurrence of a strange attractor implies global stability with local instability. Using Melnikov's method, the onset of chaotic behavior can be predicted and verified with simulation results, and finally demonstrated with the physical system. The types of chaos the system exhibits are investigated and compared.

Chapter 2

Mathematical Modeling

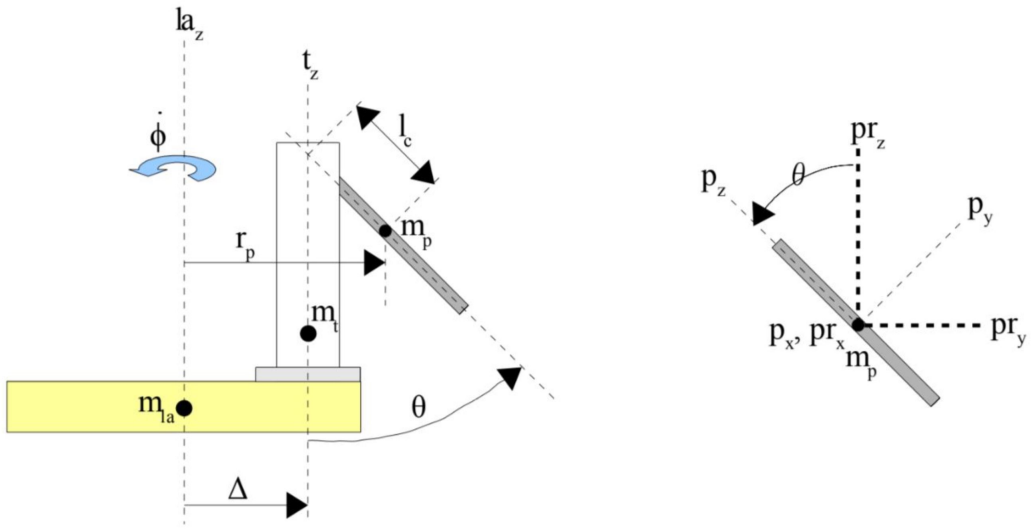

Figure 2.1: Model of the WPP system

The variables used in the modeling of the WPP system can be seen in Figure 2.1. An additional horizontal offset variable $\delta = \Delta/l$ is also used. The equations of motion for the WPP can be derived using Lagrange's equations for the Lagrangian $L = T - V$, where the kinetic and potential energy are, respectively,

$$\begin{aligned} T &= T_{rot_p} + T_{rot_t} + T_{tran_p} + T_{tran_t} \\ &= \frac{1}{2}[I_{px}\dot{\theta}^2 + (I_{py}\sin^2\theta + I_{pz}\cos^2\theta + I_{tt})\dot{\phi}^2 + m_p(\dot{\Delta} + (\Delta + l_c\sin\theta)\dot{\phi} + l_c\dot{\theta})^2 + m_t(\dot{\Delta} + \Delta\dot{\phi})^2] \\ V &= m_p g l_c(1 - \cos\theta) \end{aligned}$$

Let

$$x = (\theta \;\; \delta \;\; \dot{\theta} \;\; \dot{\delta} \;\; \dot{\phi})^T$$

$$u = (F_\Delta \;\; T_\phi)^T$$

$$v_p = x_4 + r_p x_5 + l_c x_3$$

$$r_p = x_2 + l_c \sin x_1$$

$$\dot{r_p} = x_4 + l_c x_3 \cos x_1$$

$$v_t = x_4 + x_2 x_5$$

$$I_\phi = I_{p_y} \sin^2 x_1 + I_{p_z} \cos^2 x_1 + I_{tt} + m_t x_2^2 + m_p r_p^2$$

The system dynamics can be written in state space form as:

$$\dot{x} = f(x,u) = \begin{bmatrix} x_3 \\ x_4 \\ \frac{x_5^2 \sin x_1 \cos x_1 (I_{p_y} - I_{p_z}) + m_p l_c v_p x_5 cos x_1 - m_p l_c (\dot{r}_p x_5 + r_p \dot{x}_5 + \dot{x}_4) - m_p l_c g \sin x_1 - \nu x_3}{I_{p_x} + m_p l_c^2} \\ \frac{F_\Delta - \gamma x_4}{m_p + m_t} \\ \frac{-x_3 x_5 \sin 2x_1 (I_{p_y} - I_{p_z}) - m_t v_t x_4 - m_p \dot{r}_p v_p - m_t x_2 (x_4 x_5 + \dot{x}_4) - m_p r_p (\dot{r}_p x_5 + \dot{x}_4 + l_c \dot{x}_3) - \eta x_5 + T_\phi}{I_\phi} \end{bmatrix} \tag{2.1}$$

The symbols ν, γ, and η represent damping coefficients, F_Δ is a force applied along the linear actuator, and T_ϕ is a torque applied about the vertical axis. The critical angular velocity is equal to the natural frequency of the system, ω_n:

$$\omega_c = \omega_n = \sqrt{\frac{m_p l_c g}{I_{p_y} - I_{p_z} + m_p l_c^2}} = 7.87 rad/s \approx 75.2 rpm \tag{2.2}$$

To discuss the equation of equilibria, a simpler model that does not allow variation of Δ and

$\dot{\phi}$ is used. The non-linear system dynamics become:

$$\ddot{\theta} - \omega^2 \cos\theta(\frac{3}{2}\delta + \sin\theta) + \omega_c^2 \sin\theta = -\nu\dot{\theta} \tag{2.3}$$

This dynamic model assumes that ω^2 is unaffected by the θ-dynamics, which is accurate if the inertia of the support is much larger than the inertia of the pendulum, or if the control loop prescibing ω is very "tight." This would be the case for a simulation of the dynamic system, in which the time history of ω is directly input into the system dynamics (as seen in Section 3.2.2). Equation (2.3) may be written is state space form as

$$\dot{x} = f(x,\mu) = \begin{pmatrix} x_2 \\ \omega^2 \cos x_1(\frac{3}{2}\delta + \sin x_1) - \omega_c^2 \sin x_1 - \nu x_2 \end{pmatrix} \tag{2.4}$$

where $x = (x_1,\ x_2)^T = (\theta,\ \dot{\theta})^T$ and $\mu = (\omega^2,\ \delta)^T$. Equilibria $\bar{x}$ satisfy $f(\bar{x},\mu) = 0$ or

$$\begin{aligned} 0 &= \bar{x}_2 \\ &= \omega^2 \cos\bar{x}_1(\frac{3}{2}\delta + \sin\bar{x}_1) - \omega_c^2 \sin\bar{x}_1. \end{aligned}$$

When $\delta = \omega^2 = 0$, the system reduces to the simple planar pendulum, with equilibria at $\bar{x} = (0,0)$ and $\bar{x} = (\pi,0)$. As ω^2 is increased through ω_c^2, the equilibrium $\bar{x} = (0,0)$ splits into three equilibria in a supercritical pitchfork bifurcation. The equilibrium at $\bar{x} = (0,0)$ persists while new equilibria at $\bar{x} = (\pm\arccos(\omega_c^2/\omega^2), 0)$ are introduced.

2.1 The Cusp Catastrophe

As stated previously, the downward equilibrium of the pendulum undergoes a local pitchfork bifurcation in the (ω^2, Δ) parameter space when ω increases through ω_c with $\delta = 0$. The equation of equilibria is

$$\begin{aligned} g(\bar{\theta}, \omega^2, \delta) &= 0 \\ &= \omega^2 \cos\bar{\theta}(\frac{3}{2}\delta + \sin\bar{\theta}) - \omega_c^2 \sin(\bar{\theta}) \end{aligned} \tag{2.5}$$

This equation implicitly defines an equilibrium surface $\bar{\theta} = h(\omega^2, \delta)$. For some regions in this parameter space, h is single-valued, while in others it is triple-valued. The equilibrium surface is seen in Figure 2.2. The local bifurcation is seen at $\omega = \omega_c$, as the stable equilibrium at $\theta = 0$ splits into two nonzero stable equilibria. The region in this parameter space in which both stable equilibria are present is bounded by a curve that is centered at a cusp. This is known as the cusp catastrophe [1], with the cusp located at $(\omega^2, \delta) = (\omega_c^2, 0)$. The details of the cusp are shown in Figures 2.3 and 2.4.

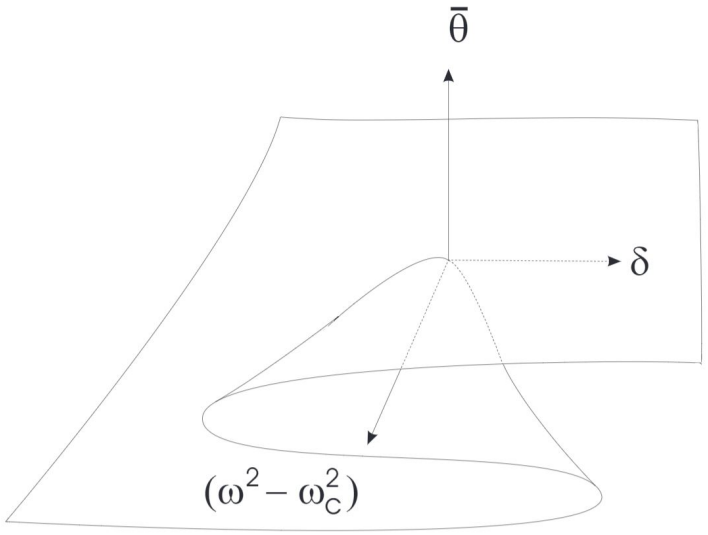

Figure 2.2: The equilibrium surface and the cusp.

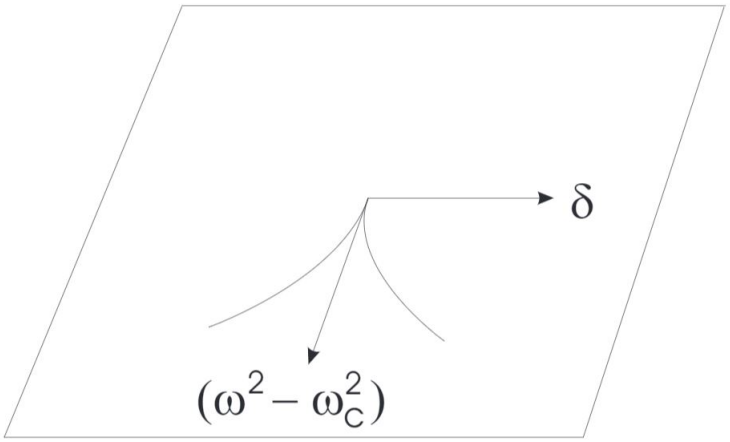

Figure 2.3: Cusp on the equilibrium plane

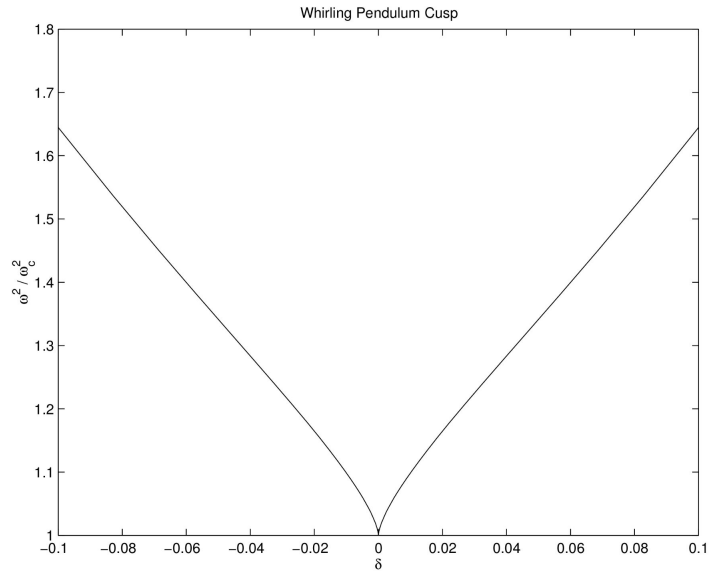

Figure 2.4: Numerical computation of the cusp

By holding one parameter constant and steadily changing the other, paths along the surface h through parameter space can be traced, and a cross section of the equilibrium space is produced. Figure 2.5 demonstrates this path for a constant $\delta = 0$ (top) and $\delta > 0$ (bottom). When $\delta = 0$, the bifurcation is clearly defined at $\omega = \omega_c$, but when there is a horizontal offset, the second stable equilibrium does not appear until some $\omega > \omega_c$. As $|\delta|$ is increased, the appearance of this equilibrium progresses further from away from ω_c. This is another

way to understand the characteristics of the cusp. Figure 2.6 demonstrates perturbations of θ as the spin rate ω is held constant. In this case, as δ is increased, the pendulum leaves the region bounded by the cusp, and the equilibrium disappears. The pendulum traces an "S" path as the θ value transitions to the only remaining stable equilibrium. In Figures 2.5 and 2.6, solid lines denote stable branches of equilibria while dashed lines denote unstable branches. These figures are also shown using experimental data in Section 4.1.

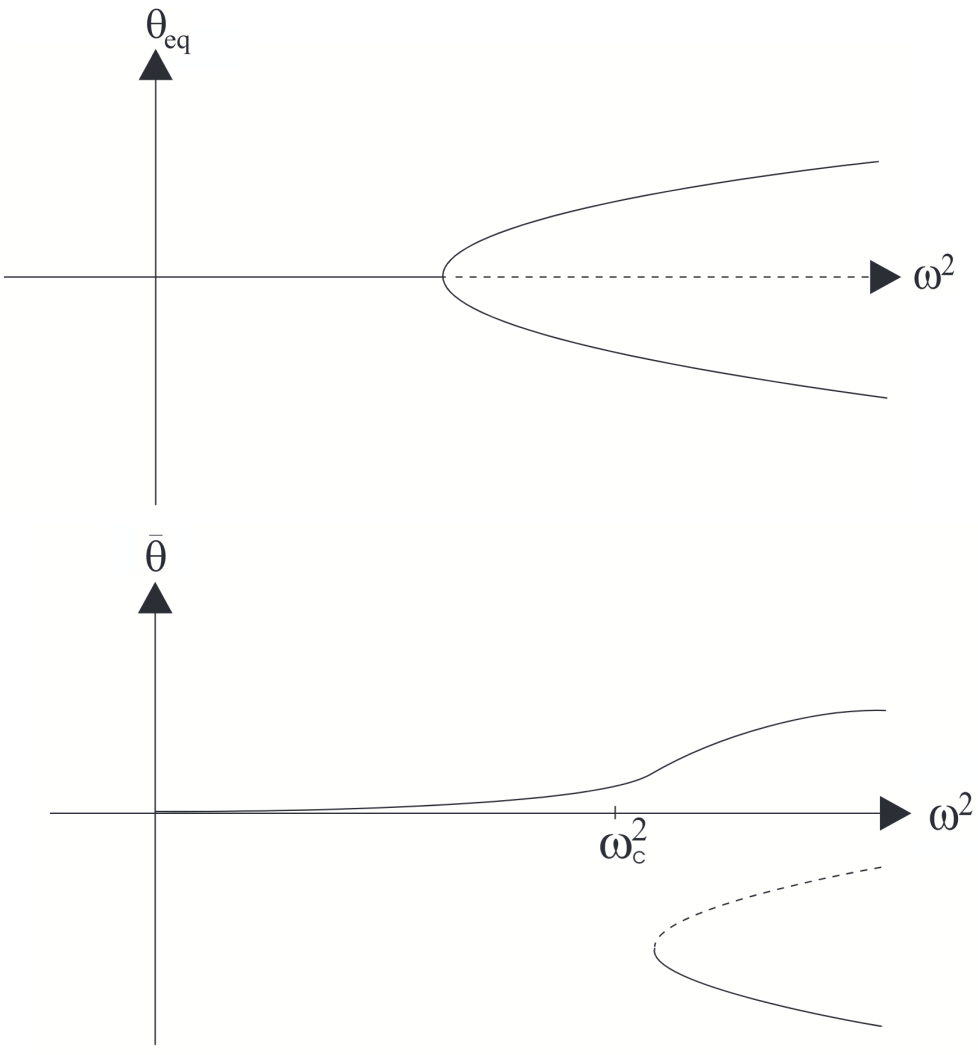

Figure 2.5: Perturbations of the pitchfork bifurcation.

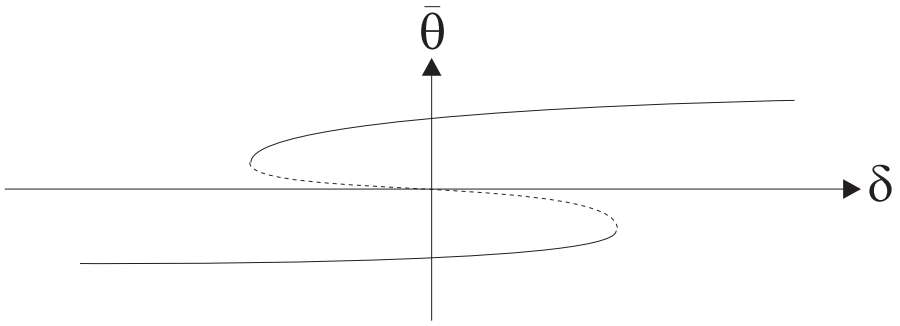

Figure 2.6: Equilibria versus δ for $\omega^2 > \omega_c^2$.

2.2 The Conservative System

When the spin rate is constant and there is no damping present ($\nu = 0$), the system is canonically Hamiltonian with

$$\mathcal{H}(\theta, p) = \frac{1}{2}p^2 + \frac{1}{2}\omega^2 \cos^2\theta - \frac{3}{2}\delta\omega^2 \sin\theta + \omega_c^2(1 - \cos\theta) \tag{2.6}$$

and $p = \dot{\theta}$ [4]. In this case, $\mathcal{H}$ is conserved, and phase portraits can be drawn at constant values of $\mathcal{H}$. These phase portraits can be seen for various values in Figure 2.7. It can be seen that the portraits are symmetrical when $\delta = 0$ and asymmetrical when $\delta \neq 0$. Furthermore, when $\omega < \omega_c$, the system is similar to that of a simple planar pendulum.

These portraits help to reveal the global homoclinic bifurcations of the WPP. These bifurcations occur when a periodic orbit intersects with a saddle point, making the periodic orbit a homoclinic orbit. The saddle equilibrium points are located at $\theta = 0$ and $\theta = \pi$, and are the intersections of the stable and unstable manifolds. The system contains two types of homoclinic orbits, and have been labeled accordingly by the authors of [7]:

- Type I - Pendulum type homoclinic orbits
- Type II - Duffing type homoclinic orbits

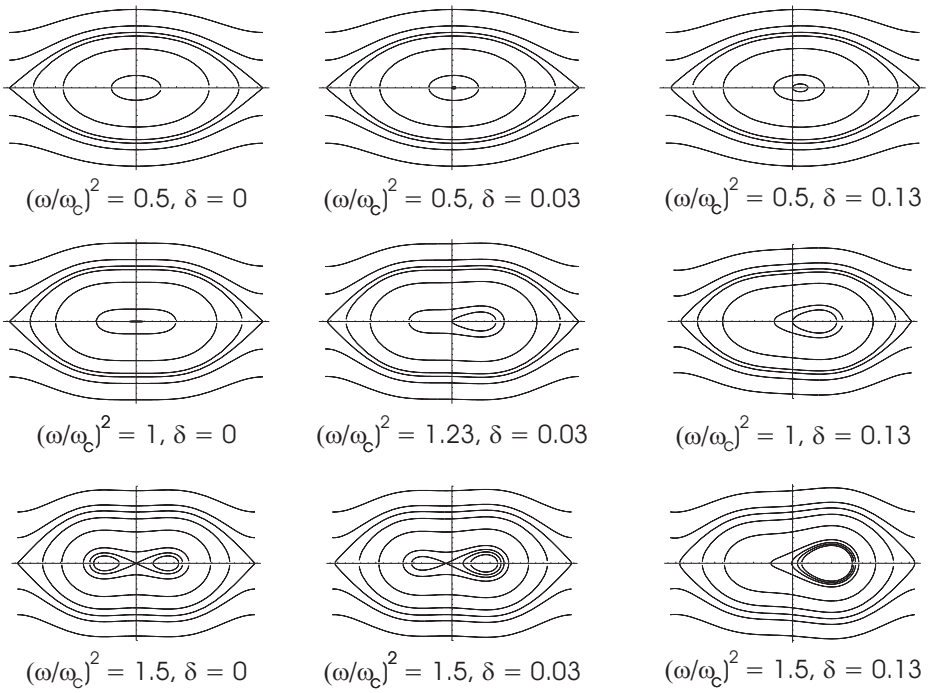

Figure 2.7: Phase portraits ($\frac{p}{|\omega_c|}$ vs θ).

The type I homoclinic orbits connect $\theta = \pi$ to itself, and can be seen as the set of outer orbits in Figure 2.8. These orbits are present in all of the phase portraits, regardless of ω. Physically, this path is visualized as the pendulum in the vertical up position, and swinging either clockwise or counterclockwise and ending in the vertical up position. The type II homoclinic orbits connect $\theta = 0$ to itself, and can be seen as the set of inner orbits in Figure 2.8. In this orbit, the pendulum can never make a full revolution (crossing $\theta = \pi$). Notice how this homoclinic orbit is only present when $\omega \geq \omega_c$.

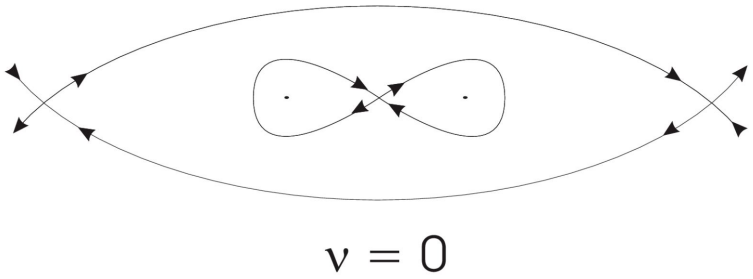

Figure 2.8: The homoclinic orbits of the WPP

2.3 Chaotic Motion

When perturbations are allowed to affect the system, chaotic motion may occur due to the global bifurcations. This is because the global bifurcations affect the system's trajectory in the phase space, and unlike local bifurcations, these changes in trajectory can not be confined to a small neighborhood. These perturbations occur in two forms: viscous damping and sinusoidal forcing. Viscous damping is always present in the physical apparatus, mostly in the form of damping in the pendulum pivot. This damping is significant, but is not enough to produce chaos in the system on its own. It is in the form of a constant multiplied by $\dot{\theta}$, the angular speed at which the pendulum is swinging. The effect of damping on the homoclinic orbits can be seen in Figure 2.9

Since ω is a parameter that can be explicitly prescribed by the experimenter, it can be chosen to have a time-varying sinusoidal portion. The sinusoidal forcing is thus appended to the input spin rate of the WPP:

$$\omega = \Omega + \epsilon\beta \sin \alpha t \tag{2.7}$$

where Ω is some nominal spin rate $\Omega > \omega_c$, and $0 < \epsilon \ll 1$. The constants α and β are parameters that determine the amplitude and frequency of the sinusoidal portion. Therefore, Ω, α, and β are all chosen inputs.

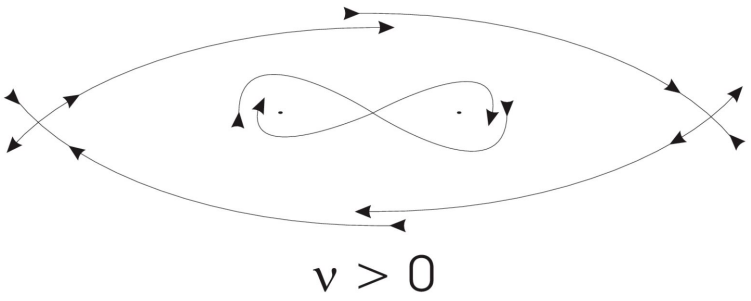

Figure 2.9: Effect of damping on the homoclinic orbits

2.3.1 The Perturbed System

When the original unperturbed equilibrium point is of the saddle type in the $(\theta, \dot{\theta})$ plane, the periodic motion that ensues is also considered of the saddle type, and represented by a saddle type fixed point, which in this case is located at either $\theta = 0$ or $\theta = \pi$. This can be seen in Figure 2.10. These saddle equilibrium points have a 2-dimensional stable manifold, and a 1-dimensional unstable manifold. When perturbations occur, the unstable manifold deviates from the stable manifold. Chaotic motion may occur when there are transverse homoclinic points (discussed further in the following section). This means that the unstable manifold intersects with the stable manifold at a non-tangent point. This can be seen in Figure 2.11. Figures 2.10 and 2.11 are adapted from [7].

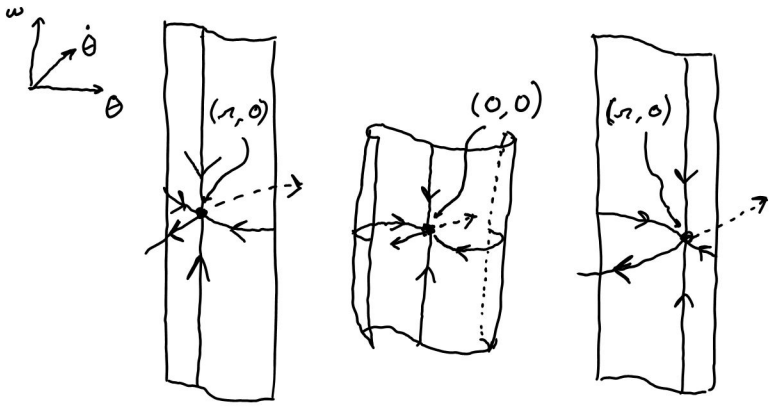

Figure 2.10: Stable and unstable manifolds of the equilibrium saddle points (adapted from [7])

2.3.2 Melnikov's Method

Using the definition of ω given in Equation 2.7, the constants α and β can be altered to determine their affect on the chaos of the system. The authors of [7] consider the ω dynamics

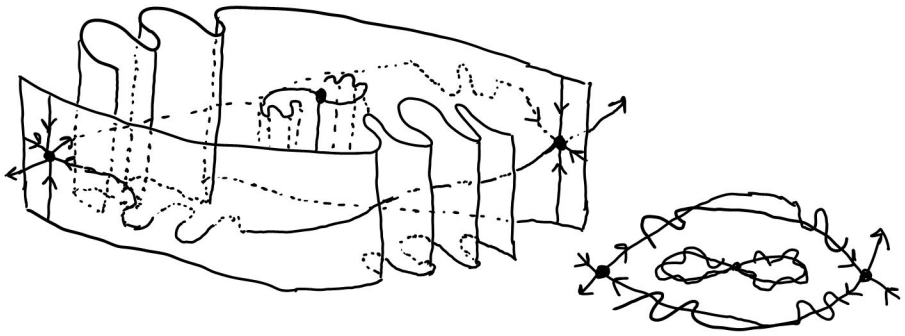

Figure 2.11: Deviation of unstable manifold due to perturbations (adapted from [7])

explicitly, however this report treats ω as a parameter, which greatly simplifies the dynamics. The offset δ is also considered to be zero in this analysis. Alternative cases in which $\delta \neq 0$ are discussed in Section 4.3.2, in order to determine if the inclusion of a horizontal offset has an effect on the onset of chaos.

Using the new definition of ω, the resulting state space equations for the θ dynamics are:

$$\begin{pmatrix} \dot{x_1} \\ \dot{x_2} \end{pmatrix} = \begin{pmatrix} x_2 \\ (\Omega^2 \cos x_1 - \omega_c^2) \sin x_1 \end{pmatrix} + \epsilon \begin{pmatrix} 0 \\ -\nu x_2 + 2\Omega\beta \sin x_1 \cos x_1 \sin \alpha t \end{pmatrix} \tag{2.8}$$

where $x_1 = \theta$ and $x_2 = \dot{\theta}$. In order to investigate this system, Poincaré maps are used, which take "snapshots" of the state of the system at time intervals with a period $T = 2\pi/\alpha$. As given by equation 4.5.16 of [2], the Melnikov function along a particular homoclinic orbit $q^0(t)$ for this system is

$$M(t_0) = \int_{-\infty}^{\infty} \left\{ -\nu x_2^2 + 2\Omega\beta x_2 \sin x_1 \cos x_1 \sin \alpha(t + t_0) \right\} (q^0(t)) dt. \tag{2.9}$$

The function $M(t_0)$ is proportional to the distance between the stable and unstable manifolds of the hyperbolic saddle point at time t_0. If at some time t_0, this equation is equal to zero

along a non-tangent path, this point is termed a transverse homoclinic point. This occurrence guarantees chaotic dynamics by the Smale-Birkhoff homoclinic theorem [2]. Furthermore, the presence of one transverse intersection reveals further information of the manifolds, as detailed by [7]:

- The existence of infinitely many transverse intersections
- The existence of three-dimensional horseshoes for the Poincaré map
  - infinitely many unstable periodic motions of arbitrarily long periods
  - infinitely many unstable nonperiodic (chaotic) motions

In effect, this means if there is one non-tangent intersection between the stable and unstable manifold ($M(t_0) = 0$ at any t_0), there will be both unstable periodic motion, and chaotic motion. This will be investigated in Chapter 5.

The authors of [7] detail a method to simplify equation 2.9 into a form that can be computed more easily. This is done by separating it into two integrals I_1 and I_2:

$$\begin{aligned} I_1 &= \int_{-\infty}^{\infty} x_2^2(q^0(t))dt \\ I_2 &= \int_{-\infty}^{\infty} x_2 \sin x_1 \cos x_1 \sin \alpha(t+t_0)(q^0(t))dt. \end{aligned}$$

I_1 is then reduced further by using the knowledge that x_2 approaches 0 exponentially as $t \to \pm\infty$, as given by the Hartman-Grobman Theorem [3]. The integral I_2 is then reduced by treating $q^0(0)$ as the midpoint of the orbit, which results in x_2 being an even function on the outer orbits ($\bar{x_1} = \pi$) and an odd function on the inner orbits ($\bar{x_1} = 0$). Now there is a different computeable I_2 for the two types of homoclinic orbits, where $q^o(t)$ represents the

outer homoclinic orbit, and $q^i(t)$ represents the inner homoclinic orbit. For the outer orbits:

$$I_{2_o} = \cos \alpha t_0 \int_{-\infty}^{\infty} x_2 \sin x_1 \cos x_1 \sin \alpha t(q^o(t))dt. \tag{2.10}$$

For the inner orbits:

$$I_{2_i} = \sin \alpha t_0 \int_{-\infty}^{\infty} x_2 \sin x_1 \cos x_1 \cos \alpha t(q^i(t))dt. \tag{2.11}$$

Applying these integrals leads to the current form of Melnikov's function:

$$M(t_0) = -\nu I_1 + 2\Omega\beta I_2 \tag{2.12}$$

The integrand of I_1 is always positive, so for the unperturbed case when $\beta = 0$ (or when β is sufficiently small), the unstable manifold is "inside" the stable manifold. Equation 2.12 gives an easy way to compute zeros for the Melnikov function. Through inspection of Equations 2.10 and 2.11, it can be seen that I_2 varies by a sinusoidal function of αt_0, and oscillates between $-|I_2|$ and $|I_2|$. If $\nu I_1 < \max(2\Omega\beta I_2)$, then there is a transverse intersection at the point t_0 when $\nu I_1 = 2\Omega\beta I_2$.

Since the onset of chaos can be predicted from $|2\Omega\beta I_2| > \nu I_1$ at *any* t_0 along the orbit, it is only necessary to check the maximum value of I_2. Thus, the terms $\sin(\alpha t_0)$ and $\cos(\alpha t_0)$ can be disregarded; it is not necessary to check each value of t_0. A transverse intersection of the manifolds of the outer orbits results in the Pendulum Type chaos (if $|2\Omega\beta I_2| > \nu I_1$ along the outer homoclinic), and a transverse intersection of the manifolds of the inner orbits results in Duffing type chaos (When $|2\Omega\beta I_2| > \nu I_1$ along the inner homoclinic).

For large enough values of β, both sets of homoclinic orbits will be perturbed enough to result in chaotic motion, theoretically allowing both types of chaos. The authors of [7] theorize that

the system could “hop” from one type of chaos to the other. However, they were unable to prove this conjecture, as the hyperbolic invariant sets associated with the homoclinic orbits are bounded apart. This topic is investigated through numerical simulation in Chapter 4.

Chapter 3

Experimental Setup

The experimental apparatus used in this report was built by Justin Ratcliff, as part of a MS degree project. The recent addition of a Real-Time Interface dSPACE Controller Board allows for better control of system. Figure 3.1 shows the apparatus.

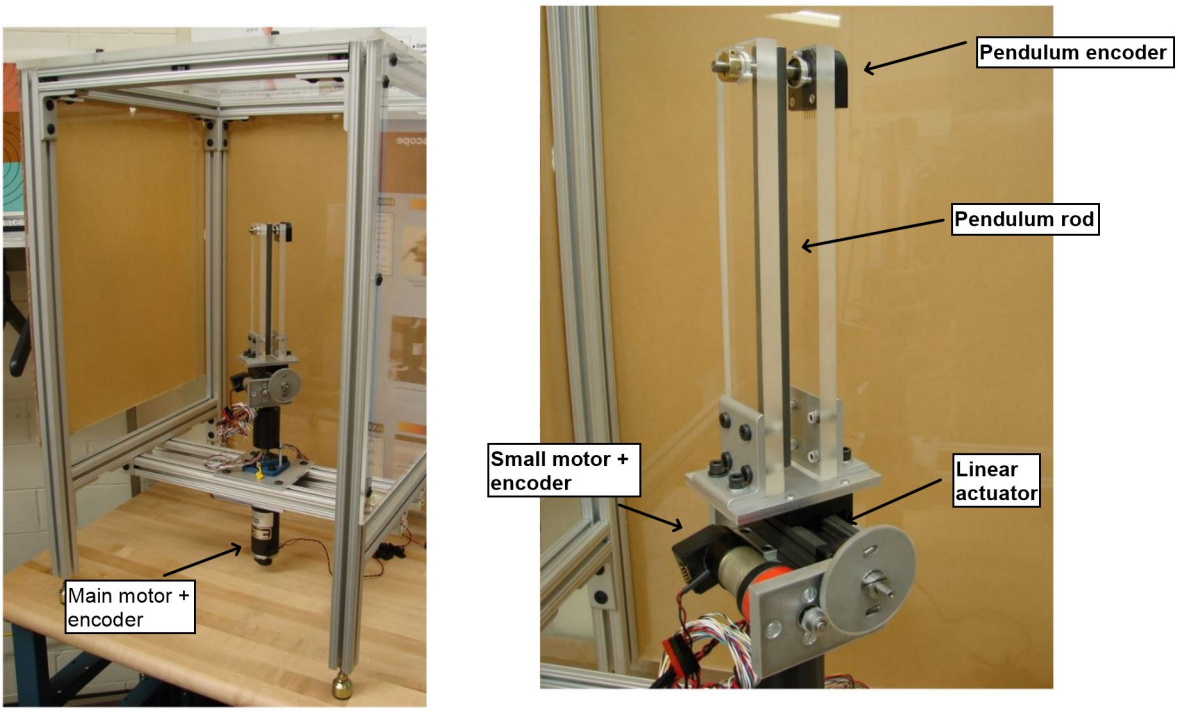

Figure 3.1: Whirling Planar Pendulum physical apparatus

3.1 Hardware

The Whirling Planar Pendulum includes a 24 volt motor that spins a 9 3/4" aluminum pendulum around the vertical axis. A smaller 24 volt motor is attached to a linear actuator to operate the horizontal displacement (offset) of the pendulum away from the vertical axis. Three optical encoders are attached, one at the pendulum pivot to measure θ, one to the linear actuator to measure Δ, and one to the main motor to measure ω. All three have 1024 counts per revolution. Two DC servo amplifiers power the motors, and receive a command signal from the dSPACE Controller Board.

Finally, but perhaps most importantly, a kill switch (which closes the motor drive circuit) is wired to the servo amplifiers, which is capable of stopping all command signals to the hardware. The switch must be held closed at all times for the pendulum to be operated, and released in cases of emergency. This switch is necessary for both safety of the user as well as safety of the system, as the main motor is powerful enough to very quickly damage or destroy the system, and to move the pendulum at speeds which could seriously injure the user. Additionally, an acryllic enclosure surrounds the system, and limiters are placed in the software to prevent too high of a command signal reaching the motors.

The encoders and amplifiers are connected to the dSPACE DS1103 PPC Controller Board. This is a real-time processor with a comprehensive I/O system. The board can accept input, and supply output, of a range ± 10 Volts. The dSPACE board receives input from the encoders, as well as powers them with a voltage of 5V and current of 1.5A. The board also supplies a command signal to the servo amplifiers, in order to control the motors.

3.2 Software

3.2.1 Apparatus Control

The dSPACE board is controlled directly through Control Desk 5.5, which is the software connected with the dSPACE board, and is operated through a graphic user interface. Control Desk receives a Simulink model, which contains the control algorithms to run the experiments. A PID controller was used to input the voltage necessary to keep the motor spinning at a specified spin rate that is specified during the experiment through the user interface. Control Desk is capable of recording data from the encoders with a time step of 0.001 seconds, and exporting it directly to MATLAB as a .mat file. Although this time step is slow compared to the rate at which the motors spin, the dSPACE board samples the data at a much faster rate, allowing the Simulink model to accurately control the system. Additionally, 1000 points of data per second is plenty to accurately model the dynamics after the experiment is finished.

The Simulink model is also equipped with a sinusoidal function which alters the spin rate by chosen amplitude β and frequency α. This can be turned on and off through the user interface. The user input is restricted by the following limits:

- Pendulum Angular Velocity: 0 to 150 rpm
- Sine Wave Amplitude: 0 to 50 rpm
- Since Wave Frequency: 0 to 20 Hz
- Horizontal Spin Axis Displacement: -10 to 10 mm

3.2.2 Simulation

A simulation was created using MATLAB in order to model behavior of the pendulum for experiments that either require unreasonable time periods, or could result in damage to the system. This allows for results to be quickly obtained that would have required hours of operation of the physical system. The simulation uses an Euler forward approximation on the state space model for time steps of 0.001 seconds. The time step was chosen in order to match the time step of recorded data from the physical apparatus. In this way, a physical experiment can be run, and the recorded angular velocity time history can then be applied to the simulation. The simulation outputs a time history of the pendulum angle, as well as a Poincaré map by plotting the data points representing the system's state at every time step $T = 2\pi/\alpha$.

The author of [7] used a physical setup in which the input to the system is a voltage, which directly corresponds to the torque applied about the vertical axis. However, this system did not include Δ as a variable, and thus the moment of inertia of the frame was constant. In the system used for this report, the pendulum frame is on a linear actuator, and thus the frame's moment of inertia is dependent on Δ. Therefore, a control algorithm is used to apply voltage in order to set ω to a specific spin rate. In the simulation, ω is directly prescribed as a vector containing the time history of ω. It then follows that ω is not affected by the θ-dynamics, and the simplified dynamic model of equation 2.3 is confirmed. Even though the control system of the physical system is able to control ω to a very low error, the simplified model becomes an approximation.

The damping constant ν was set to match the damping in the physical system as closely as possible. This was done experimentally, by recording the time history of the physical pendulum being sped up past ω_c. The same ω history was applied to the simulation with a

damping coefficient of 0, and the time histories were compared, as seen in Figure 3.2. Plot (a) shows the time history of the physical system and plot (b) shows the simulation with a matching damping coefficient. Plot (c) shows the simulation with no damping.

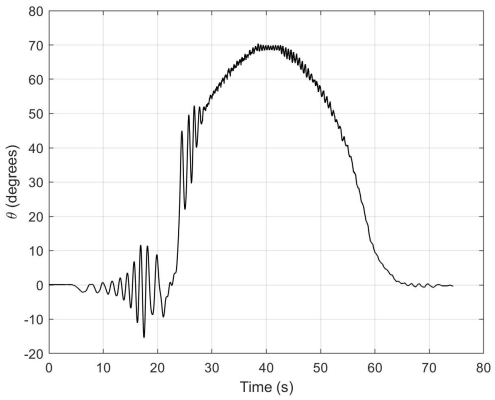

(a) Physical Apparatus

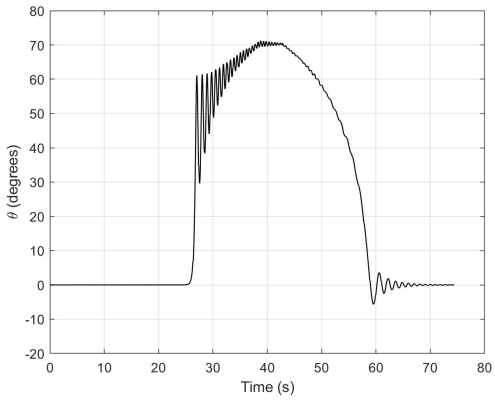

(b) Simulation

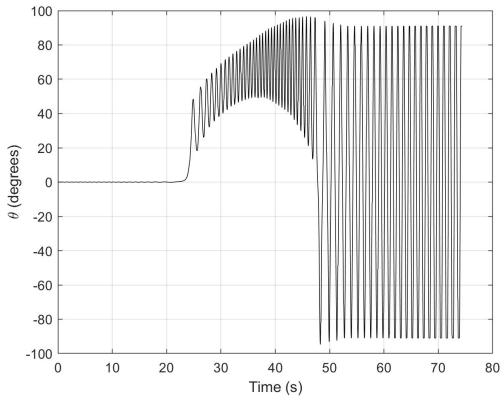

(c) Simulation

Figure 3.2: Comparison between results from the physical system and the simulation with different damping coefficients.

Chapter 4

Results

This chapter details the results of the experimental and numerical investigation into the Whirling Planar Pendulum. Section 4.1 details insight into the cusp catastrophe associated with local bifurcations in the two-dimensional parameter space of the system. Experimental modeling of the equilibrium manifold over parameter space is generated by testing the equilibrium path through the phase space. Section 4.2 investigates the system's path through phase space. Section 4.3 is a study into the chaotic oscillations exhibited by the system. This includes analytical results of Melnikov's method, as well as simulation results.

4.1 Physical Modeling

In an attempt to verify the analytical results obtained in in Chapter 2, the physical system was used to model the equilibrium paths, similar to the numerically generated plots in Figures 2.5 and 2.6. These experimental plots can be generated due to the ability of the system to change horizontal displacement (Δ) during the experiment. Otherwise, at a position $\Delta > 0$ the pendulum will tend to only swing in the positive direction as the spin rate is increased smoothly from zero. In order to locate the negative equilibrium value, the pendulum needs to already be at a negative θ value before the specified parameters are met. This is done most intuitively by first setting Δ to a negative value and speeding ω up to the specified spin rate. The parameter Δ is then increased until it reaches the specified positive displacement.

If this is done slowly and steadily, the pendulum will remain at its negative equilibrium. This transition can be seen in Figure 4.1. The unstable portion of the transition is not shown in plot (b), since this plot is derived from experimental data. Figure 4.2 shows the equilibrium path at constants of $\Delta = 0$ and $\Delta = 5mm$, respectively, as ω is increased. The pendulum does not have a "preferred" equilibrium value when $\Delta = 0$, as the equilibrium path splits at the same point, and each path is equally likely to occur.

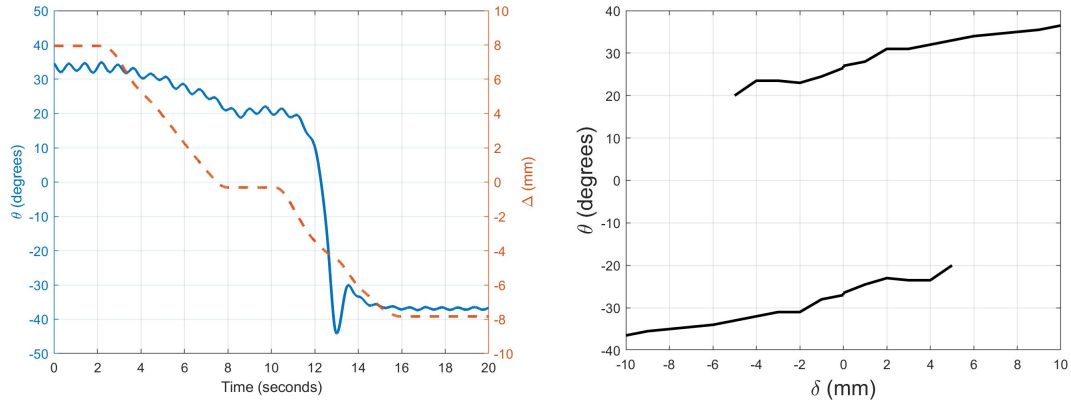

Figure 4.1: Experimental data showing equilibria versus Δ for $\omega^2 > \omega_c^2$

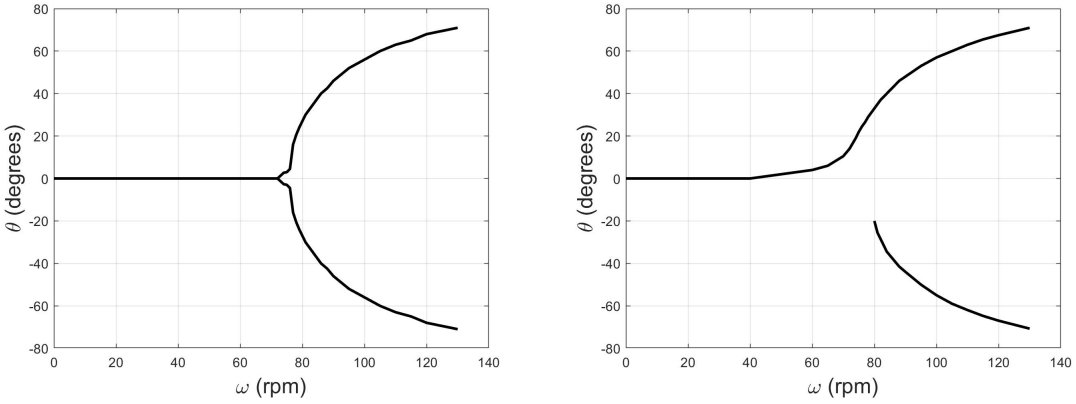

Figure 4.2: Experimental data showing the pitchfork bifurcation of the θ equilibrium for an offset of $\Delta = 0$ mm (left) and $\Delta = 5$ mm (right)

A quicker and more "brute force" approach to obtain both sets of equilibrium points is to

constrain the pendulum into the positive or negative side. This can be done by simply putting a small piece of tape or string in the way, preventing the pendulum from swinging to the other side. This is the method that was used to obtain the full set of data, due to setup speed and the ability to precisely choose Δ before the motor is spinning. By obtaining values of a range of $-10mm < \Delta < 10mm$ and $0 < \omega < 130rpm$, the full equilibrium surface can be mapped to the extent of the capabilities of the system. This can be seen in Figure 4.3. The cusp is not explicitly shown in this figure, however it can be seen that there is only one equilibrium at certain values of ω and Δ, when $\omega > \omega_c$.

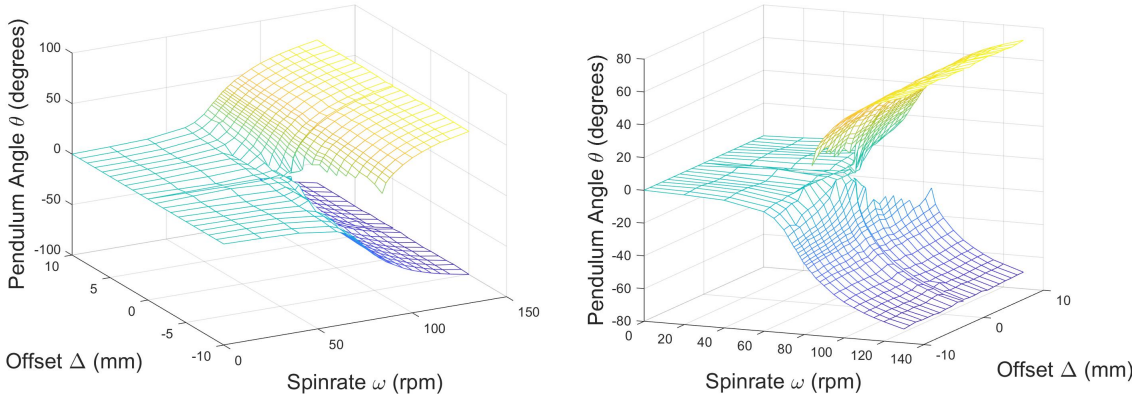

Figure 4.3: Whirling Planar Pendulum physical apparatus

4.2 The Phase Space

As explained in Section 2.2, the phase portraits of the system are dependent on ω and δ, and were created by plotting lines of constant $\mathcal{H}$. In an attempt to replicate the shape of the phase portraits using simulation data, a single trajectory through the $(\theta,\dot{\theta})$ plane was recorded. In order for the pendulum to trace the lines for the level sets of $\mathcal{H}$, a sinusoidal input was applied to each specified spin rate. This caused the pendulum to "jump" between each of

the lines of constant $\mathcal{H}$. After the simulation was run for a long enough time, the pendulum has traced out the general shape of these level sets. Figure 4.4 shows these trajectory plots, and the shapes can be compared with Figure 2.7. It is important to note that these plots generated from the simulation's trajectory are not phase portraits, they just show a path through phase space. However, by applying the same parameters as in the mathematically generated phase portraits, it can be shown that the pendulum tends to follow these paths of constant $\mathcal{H}$. These plots are not completely level as seen in Figure 2.7 because damping was present in the simulation, while the Hamiltonian requires the system to be conservative ($\nu = 0$).

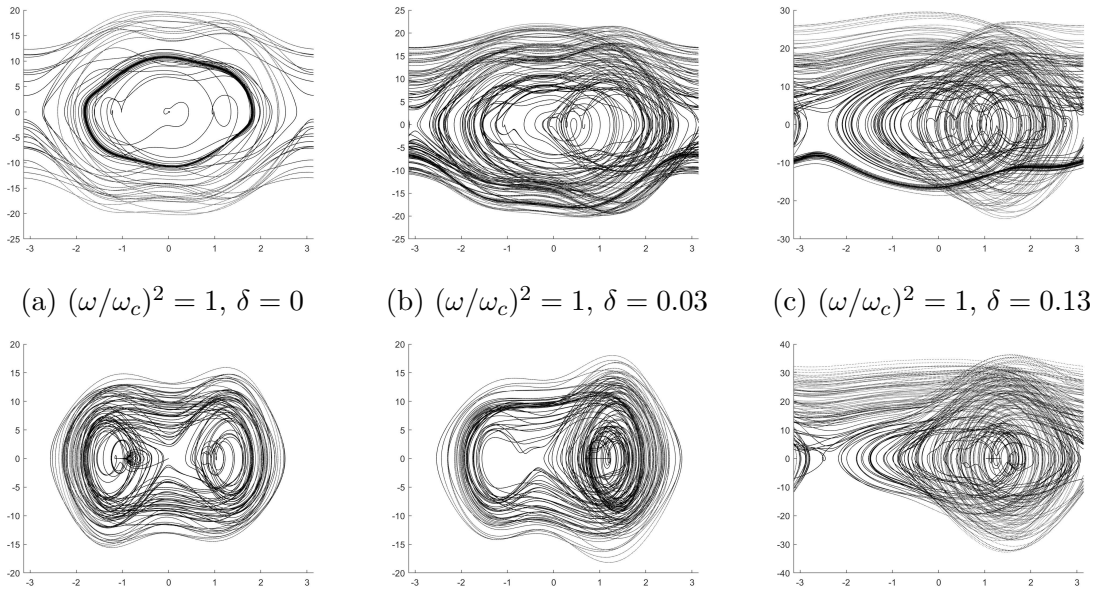

(a) $(\omega/\omega_c)^2 = 1$, $\delta = 0$ (b) $(\omega/\omega_c)^2 = 1$, $\delta = 0.03$ (c) $(\omega/\omega_c)^2 = 1$, $\delta = 0.13$

(d) $(\omega/\omega_c)^2 = 1.5$, $\delta = 0$ (e) $(\omega/\omega_c)^2 = 1.5$, $\delta = 0.03$ (f) $(\omega/\omega_c)^2 = 1$, $\delta = 0.13$

Figure 4.4: Simulation trajectory plots through phase space, showing paths similar to the numerically derived phase portraits

4.3 Chaotic Motion

In an attempt to predict the onset of chaotic motion, Melnikov's method was used. Physically, this provides a range of α and β values that cause intersections in the stable and unstable manifolds of a homoclinic saddle point. It was concluded in [6] that Melnikov's method provided a "lower bound" for the sinusoidal parameters that cause chaotic motion for a magnetic pendulum. This means that all the simulations that showed evidence of chaos had α and β values that were within the parameter region that Melnikov's method predicted to have chaotic motion. This assessment can be tested with the Whirling Planar Pendulum to see if similar conclusions can be made. However, this investigation does not give insight into the validity of Melnikov's method, as the theorems presented in Section 2.3.2 apply to the conservative system. The analysis in this report instead attempts to test the viability of the Melnikov's method prediction for the WPP system after damping is included (non-conservative system). In order to do this, the results from Melnikov's method using integer steps from $0 \leq \alpha \leq 50$ and $0 \leq \beta \leq 100$ were compared with simulations run with integer steps of parameter values $0 \leq \alpha \leq 30$ and $0 \leq \beta \leq 50$.

Since the two homoclinic orbits are separate bounded sets, this analysis can be done for both orbits, giving an understanding of the onset of both types of chaos. It is unreasonable to attempt to develop these boundaries using data from the physical system, as each experiment would take close to an hour to receive enough data, and could potentially damage the system.

4.3.1 Comparison of Melnikov's Method and Simulation Results

The analysis done in Chapter 4 provides a straightforward criterion for when Melnikov's distance predicts the onset of chaos. However, the numerical analysis ended here because this still required integration along the homoclinic orbit. Using the simulation, these orbits

are able to be isolated by inspecting the phase map to determine a point in time in which the pendulum's periodic orbit intersected with the saddle equilibrium point. The values of θ and $\dot{\theta}$ along the orbit could then be gathered. With data points at very small time intervals, Matlab can be used to easily compute these integrals and check for zeros in Equation 2.12. Figure 4.5 shows the isolated inner homoclinic orbit that was used for these calculations.

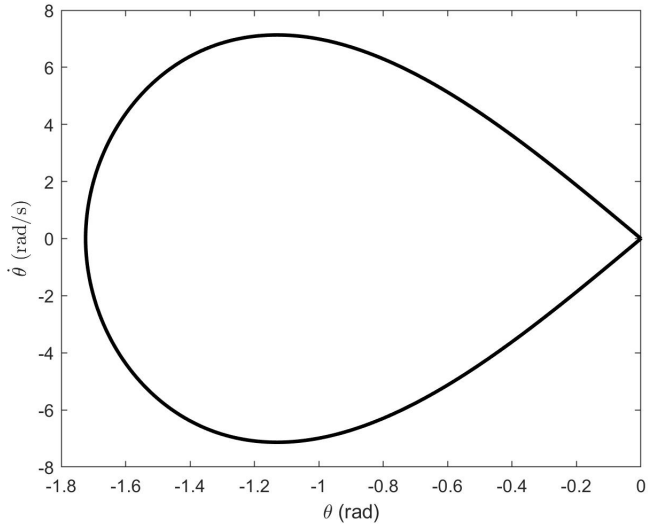

Figure 4.5: Homoclinic orbit from simulation used in calculations for Melnikov's method for Duffing Type chaos

Figure 4.6 shows the results of Melnikov's method for the inner homoclinic orbit on the (α,β) parameter space. It can be seen that this method results in two "clusters" of chaotic motion that do not intersect at sinuisoidal amplitudes of up to $\beta = 100$. By running the simulation for α and β values within the boundary, chaotic motion can be seen by checking the Poincaré map for evidence of a strange attractor. Figure 4.7 shows two plots, the zoomed in portion of the time history for a simulation with non-chaotic parameters ($\alpha = 3$ and $\beta = 30$), and the simulation's Poincaré map. This Poincaré map does not show a strange attractor, and thus there is no evidence of chaotic motion. Instead, it shows a normal attractor, in which the system tends to evolve towards the equilibrium value. These plots can be compared

to a simulation that exhibits Duffing Type chaos in Figure 4.8 ($\alpha = 10$ and $\beta = 30$). In this case, the Poincaré map reveals a strange attractor, in which nearby points of time step $T = 2\pi/\alpha$ may diverge arbitrarily far apart after some number of iterations, while still staying within the attractor. These same parameters were applied to the physical system, in order to gain experimental data to compare with the simulation data. The plots computed from experimental data are shown in Figure 4.9; although the experiment was only run for 300 seconds, the Poincaré map still shows part of a strange attractor. Each simulation in the range of parameter values was inspected for a strange attractor, and the simulations showing evidence of chaotic motion were recorded. The results detailing the points in which chaotic motion was observed are seen in blue on top of the Melnikov's method results (shown in black) in Figure 4.10. It is important to note that the edges of the chaotic regions in parameter space are not assumed to be smooth. These boundaries are often fractal in nature, as seen in other dynamic systems [5].

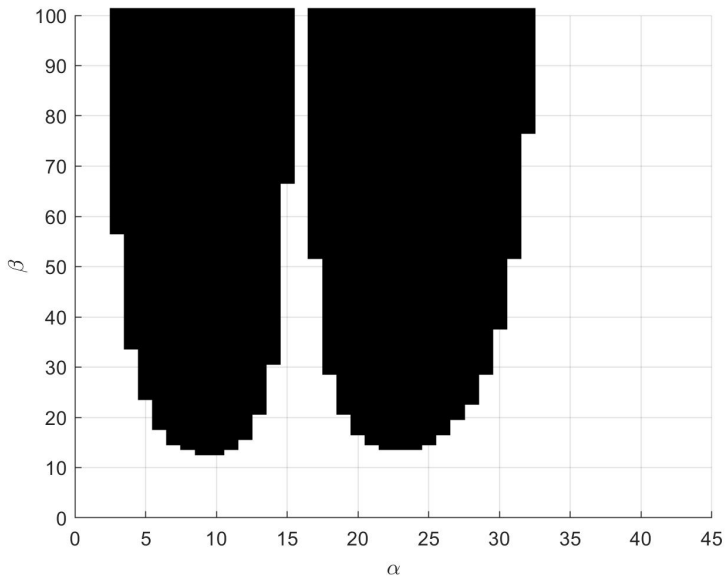

Figure 4.6: Melnikov's Method results, showing Duffing Type chaos from intersections of the inner homoclinic orbit

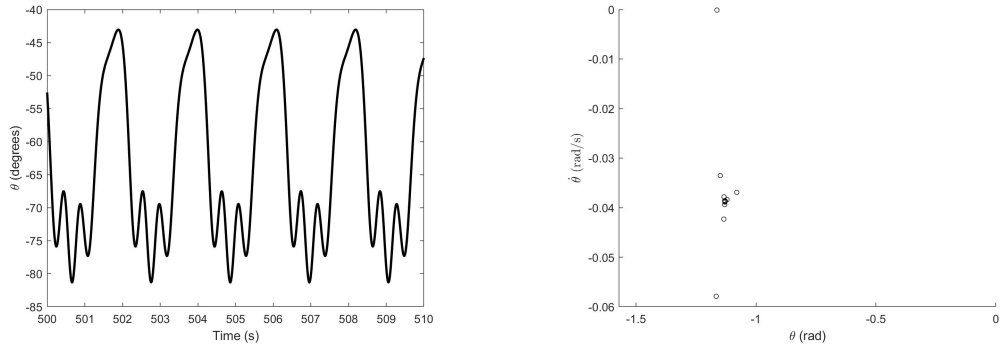

(a) Zoomed in time history (b) Poincare Map

Figure 4.7: Simulation Results for sinusoidal parameters without chaos

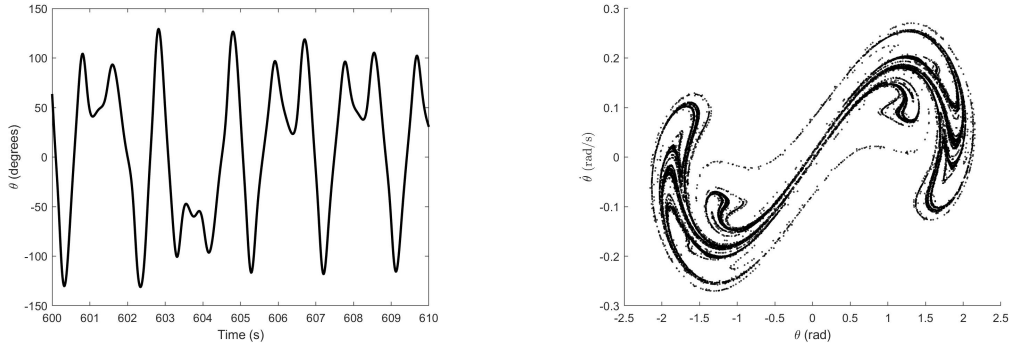

(a) Zoomed in time history (b) Poincaré Map

Figure 4.8: Simulation Results for sinusoidal parameters showing Duffing Type chaos

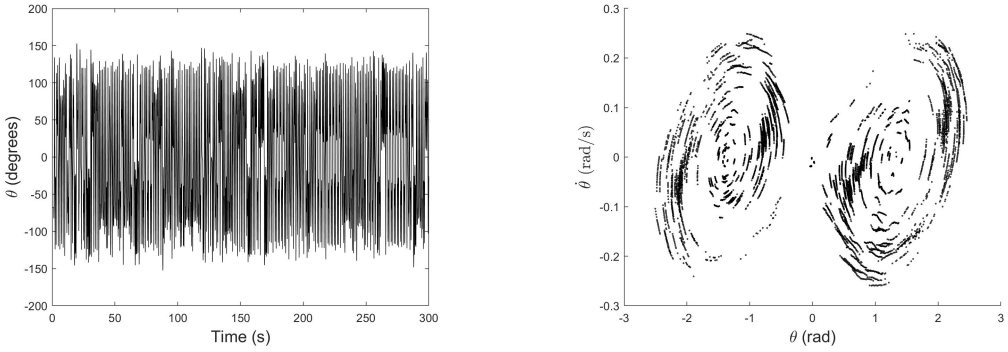

(a) Time history (b) Poincaré Map

Figure 4.9: Experimental Results for sinusoidal parameters showing Duffing Type chaos

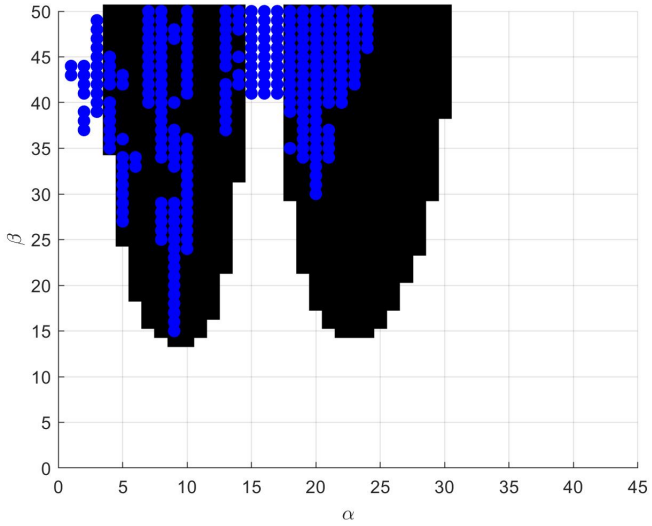

Figure 4.10: Onset of Duffing Type chaos from simulations. Shown on top of Melnikov's method's prediction

The same process was done to investigate the outer homoclinic orbit, shown in Figure 4.11. This complete orbit is only shown as a semicircle, because this connects the vertical up position to itself through the negative θ direction. If the pendulum were to swing in the positive direction, the orbit would be in the upper half of the plot. Results from Melnikov's method can be seen in Figure 4.12a. Once again, the results from the simulations can be seen in blue on top of Melnikov's method in Figure 4.12b.

In general, this Pendulum Type chaos requires greater values of β, which is expected as it would require more energy for the pendulum to spin fast enough to complete a full revolution. Figure 4.13 shows the zoomed in time history plot along with the Poincaré map for this Pendulum Type chaos ($\alpha = 20$ and $\beta = 80$) from simulation data. The sinusoidal amplitude required was too large to be ran with the physical system to obtain experimental data. This chaotic behavior involves the pendulum spinning in the same direction for extended periods of time, so a new time history plot is generated that can show total revolutions of the pendulum, and is shown as plot (a). At many of the parameter values in which Pendulum

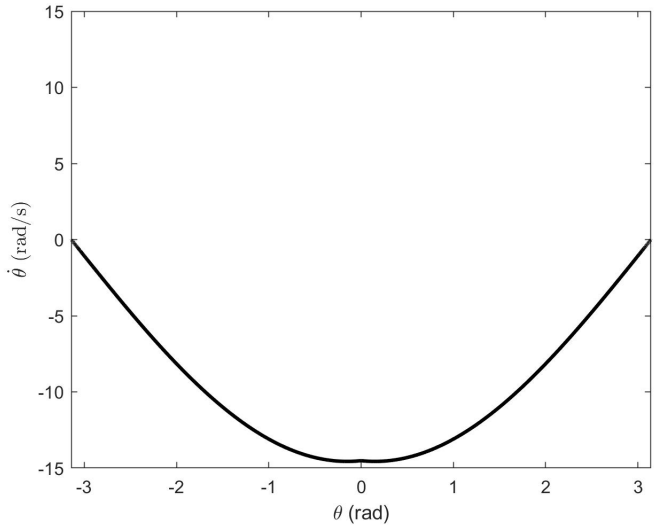

Figure 4.11: Homoclinic orbit from simulation used in calculations for Melnikov's method for Pendulum Type chaos

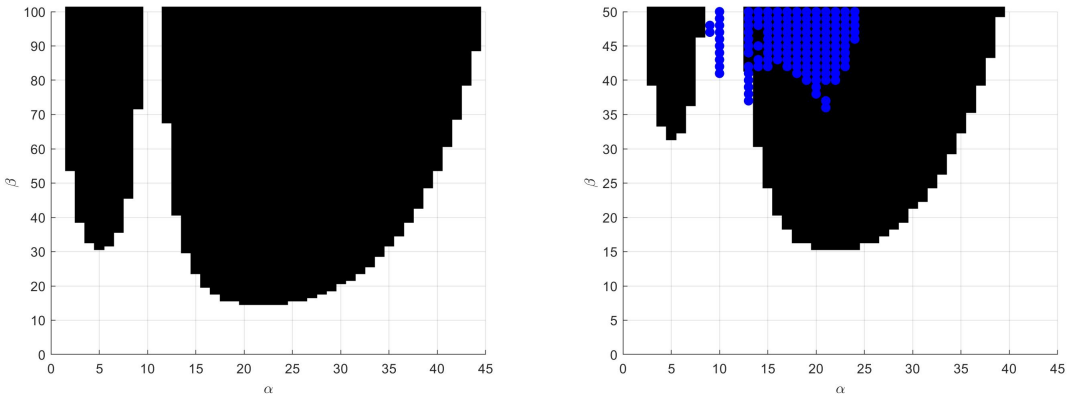

(a) Melnikov's Method results (b) Simulation results

Figure 4.12: Onset of Pendulum Type chaos, from intersections of the outer homoclinic orbit

Type chaos is possible, the Duffing Type chaos is also possible. These Poincaré maps can be differentiated in that the Duffing Type chaos leads to maps that do not reach values of $\theta = \pm\pi$, while Pendulum Type maps extend past this. The Pendulum Type maps must be 2π periodic in θ. The parameters chosen for Figure 4.13 are within the boundaries for both types of chaos, but it only exhibits Pendulum Type chaos due to the large β value.

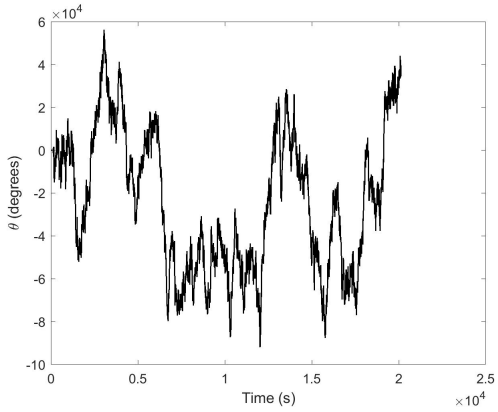

(a) Full time history

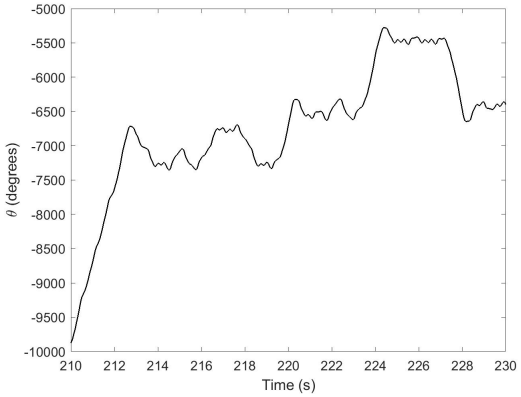

(b) Zoomed in time history

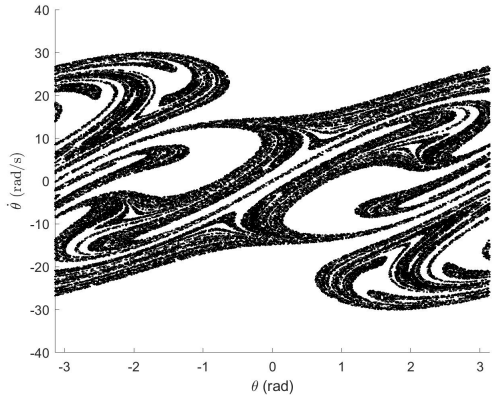

(c) Poincaré Map

Figure 4.13: Simulation Results for sinusoidal parameters showing Pendulum Type chaos

There are regions in the (α,β) parameter space that Melnikov's method predicts could show both types of chaotic motion. This provides evidence for the theory described in [7] that there are points in which both types of chaos are possible, and that the system can "hop" between them. Some simulations in these regions displayed evidence of both types of chaos. One of these simulations, with parameters of $\beta = 48$ and $\alpha = 9$ is shown in Figure 4.14. It can be seen that the simulation seems to show Duffing Type chaos in certain "blocks" of time, which are separated by instances of the pendulum swinging through at least one full revolution. This is typical of Pendulum Type chaos. The zoomed in portion of the time history shows that the motion does look very similar to simulations with only Duffing Type

chaos. This particular simulation exhibits much more Duffing Type than Pendulum Type chaos. In fact, the Pendulum Type portions of the chaotic motion are overshadowed such that they do not appear on the Poincaré map (points on the Poincaré map do not reach $\pm\pi$). Figure 4.15 shows the opposite ($\alpha = 14$ and $\beta = 50$); this simulation initially appears to be purely Pendulum Type chaos, but after zooming in, small amounts of Duffing Type chaos are present. This simulation's time history can be compared to that of the simulation from Figure 4.13, which exhibits only Pendulum Type chaos.

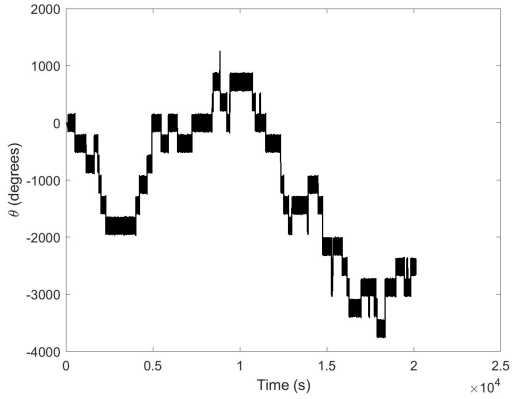

(a) Full time history

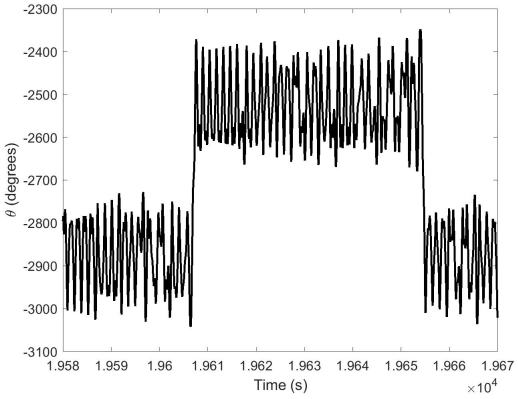

(b) Zoomed in time history

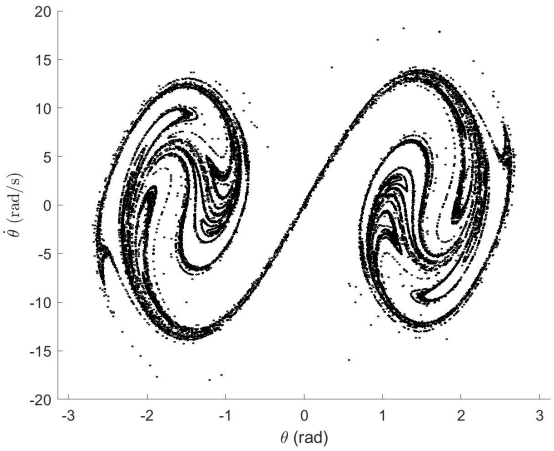

(c) Poincaré Map

Figure 4.14: Simulation Results for parameters showing mostly Duffing and some Pendulum Type chaos

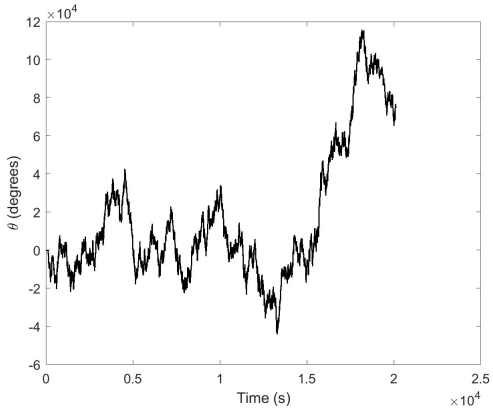

(a) Full time history

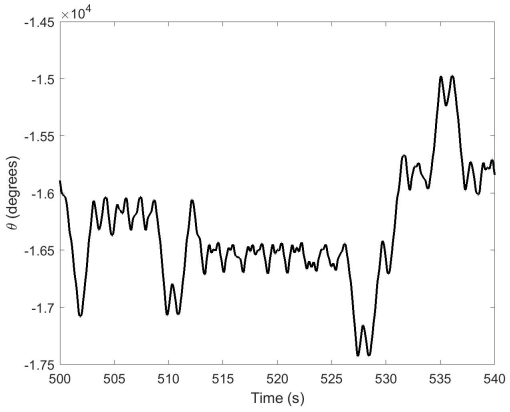

(b) Zoomed in time history

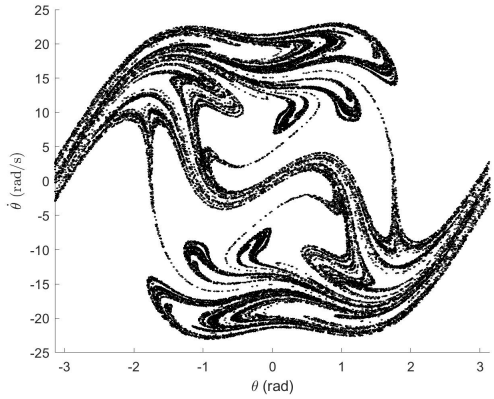

(c) Poincaré Map

Figure 4.15: Simulation Results for parameters showing mostly Pendulum and some Duffing Type chaos

Finally, a third simulation showing both types of chaos can be seen in Figure 4.16. This simulation exhibits approximately equal amounts of Duffing and Pendulum Type chaos ($\alpha = 15$ and $\beta = 48$). The unique aspect of this simulation is that by looking at simulations with similar α and β parameters, the Poincaré map can be separated into its respective parts. Figure 4.17 shows the simulation of $\alpha = 15$ and $\beta = 41$ (slightly smaller β), which has Duffing Type chaos. Figure 4.18 shows the simulation of $\alpha = 15$ and $\beta = 65$ (slightly larger β), which has Pendulum Type chaos. It can be seen that the Poincaré maps of these two simulations roughly make up the Poincaré map of Figure 4.16. They do not match

exactly, especially the Pendulum Type Poincaré map, since the change in β is large enough to affect the image. Figure 4.19 shows the regions of parameter space with the portions of Melnikov's method results from the inner and outer homoclinic orbits that are overlapping. The parameters that showed both types of chaos in the simulations on displayed on top in another plot in blue.

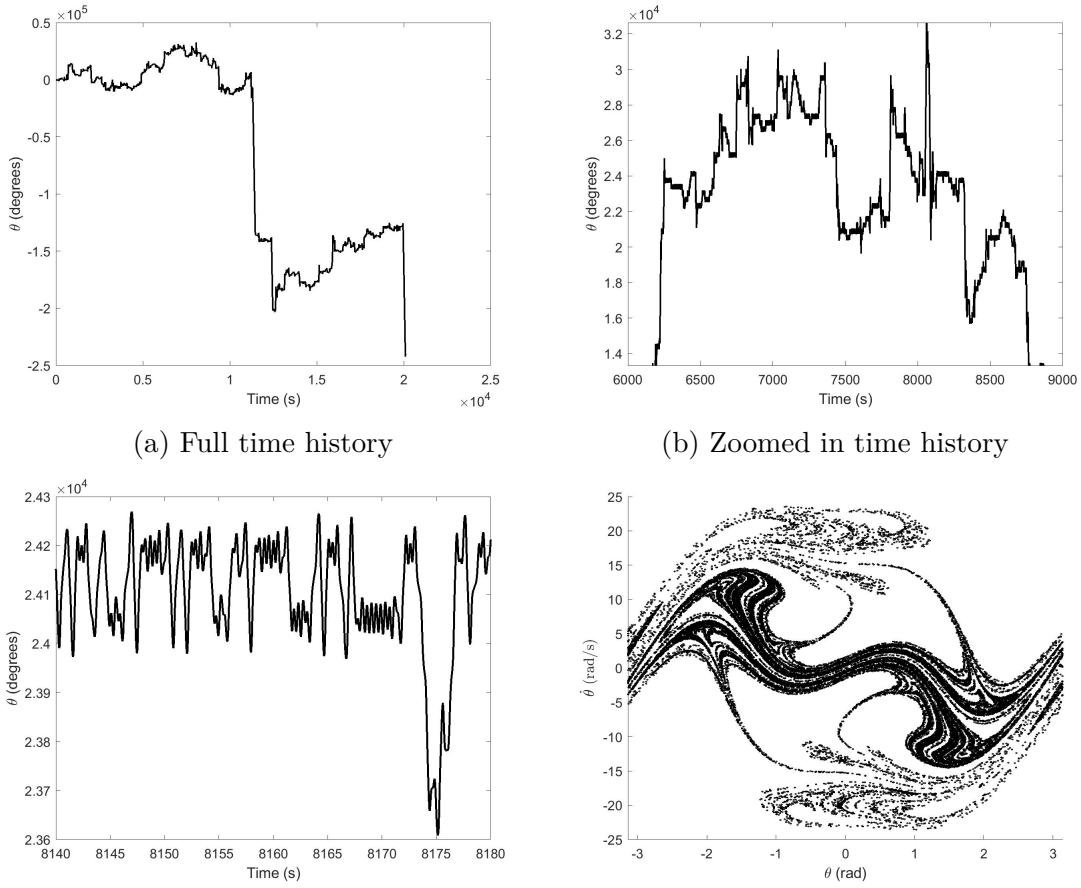

(a) Full time history

(b) Zoomed in time history

(c) Zoomed in time history

(d) Poincaré Map

Figure 4.16: Simulation Results for parameters showing equal amounts of both Duffing and Pendulum Type chaos

Next, these parameter values were tested with the physical system to see if it could also show signs of both types of chaos. An experiment was run with parameters $\alpha = 12$ and $\beta = 50$, which were at the limits of what the experimental setup could experience without possibility

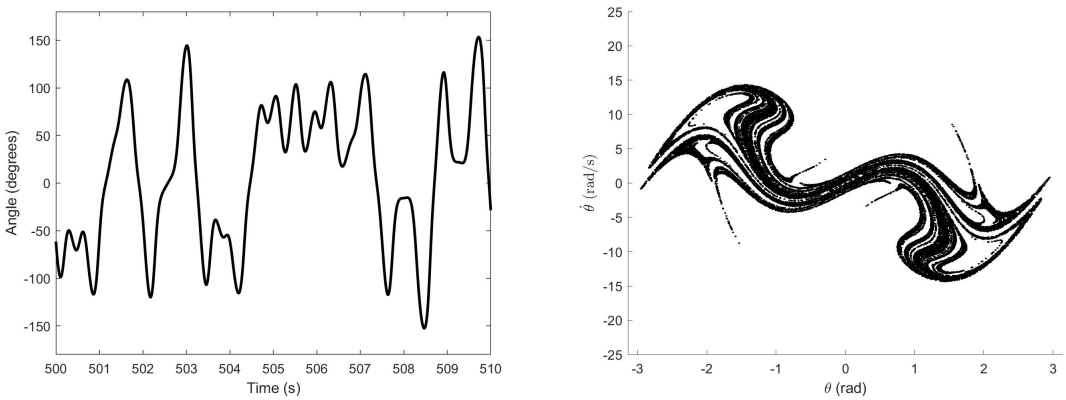

(a) Full time history (b) Poincaré Map

Figure 4.17: Duffing Type portion of Poincaré map

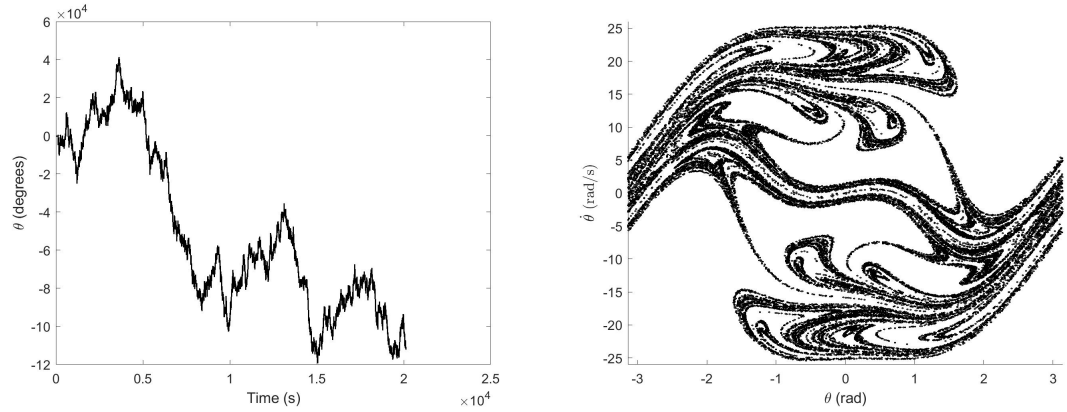

(a) Full time history (b) Poincaré Map

Figure 4.18: Pendulum Type portion of Poincaré map

of damaging the system. The results from this experiment appear in Figure 4.20. Just like with the simulation results, the time plot shows period of time where the pendulum does not make a full revolution, and periods where the pendulum spins at least one time around. Also, even with limited data points, there appears to be portions of the Poincaré map that do not reach $\pm\pi$ (Duffing Type chaos), and portions that do reach $\pm\pi$ (Pendulum Type chaos). This Poincaré map appears to show similar characteristcs as the Poincaré map from Figure 4.14.

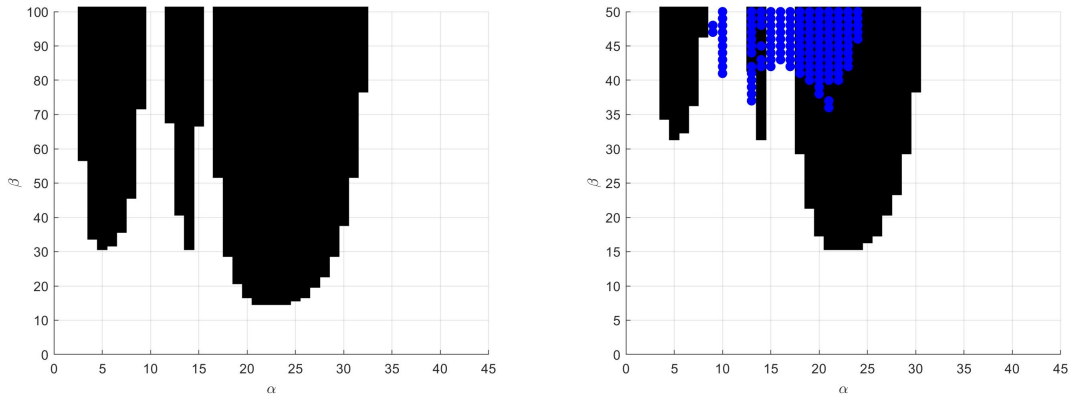

(a) Melnikov's method prediction (b) Simulation results

Figure 4.19: Onset of chaotic motion showing characteristics of both types of chaos

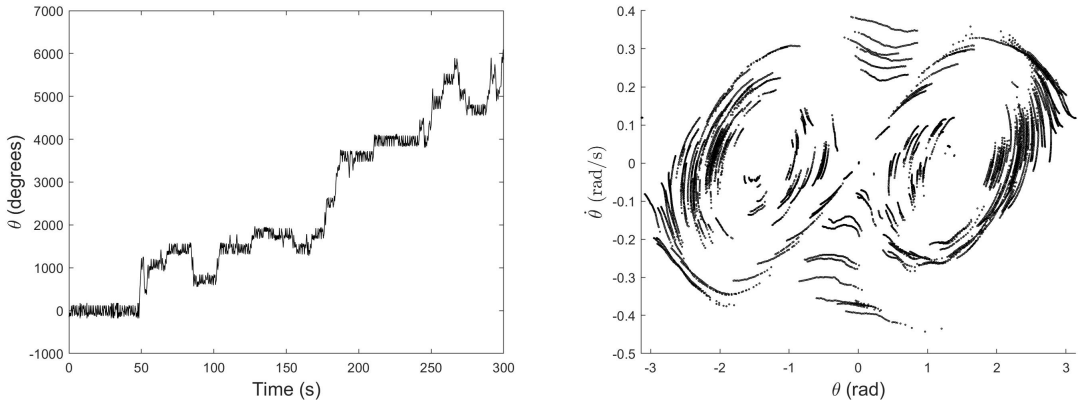

(a) Full time history (b) Poincaré Map

Figure 4.20: Experimental Results for sinusoidal parameters showing both types chaos

4.3.2 Chaos With Horizontal Offset

The analyses done up to this point were all done assuming no horizontal offset ($\delta = 0$). This section investigates the effect of δ on the onset of chaotic motion. By keeping the δ term in equation 2.5 when substituting the definition for ω while deriving Melnikov's equation,

equation 2.8 becomes:

$$\begin{pmatrix} \dot{x_1} \\ \dot{x_2} \end{pmatrix} = \begin{pmatrix} x_2 \\ \Omega^2 \cos x_1 \frac{3}{2}\delta + (\Omega^2 \cos x_1 - \omega_c^2) \sin x_1 \end{pmatrix} + \epsilon \begin{pmatrix} 0 \\ -\nu x_2 + 2\Omega\beta \sin \alpha t \cos x_1 (\sin x_1 + \frac{3}{2}\delta) \end{pmatrix} \quad (4.1)$$

By ignoring second order ϵ terms a new form for Melnikov's distance is obtained:

$$M(t_0) = \int_{-\infty}^{\infty} \left\{ -\nu x_2^2 + 2\Omega\beta x_2 \cos x_1 \sin \alpha(t + t_0)(\sin x_1 + \frac{3}{2}\delta) \right\} (q^0(t))dt. \quad (4.2)$$

Fortunately, the new term does not require much additional manipulation to obtain a form Matlab can compute. The resulting equations for I_2 are:

$$I_{2_o} = \cos \alpha t_0 \int_{-\infty}^{\infty} x_2 \cos x_1 \sin \alpha t (\sin x_1 + \frac{3}{2}\delta)(q^o(t))dt.$$

$$I_{2_i} = \sin \alpha t_0 \int_{-\infty}^{\infty} x_2 \cos x_1 \cos \alpha t (\sin x_1 + \frac{3}{2}\delta)(q^i(t))dt.$$

This new form was used in the same procedure as in the previous section to predict chaos. The new boundary for both types of chaos with a horizontal offset of $\delta = -.12$ can be seen in Figure 4.21. The results from one simulation with parameters $\alpha = 10$ and $\beta = 30$ are also shown in Figure 4.22. In general, The horizontal displacement seems to dampen chaotic motion with low values of α, and strengthen chaotic motion with high values of α. By looking at the time history of the simulation, it can be seen that the pendulum spins further into the direction of the offset, and the Poincaré map is skewed towards this same direction.

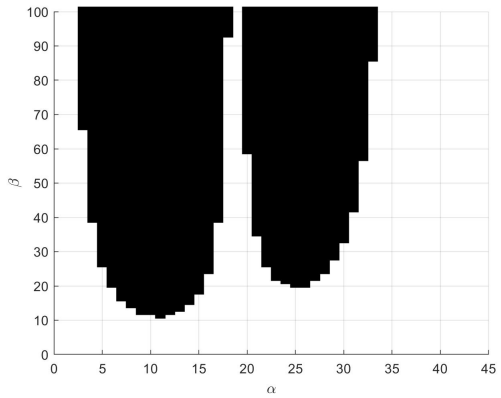

(a) Melnikov's results for Duffing chaos with horizontal displacement

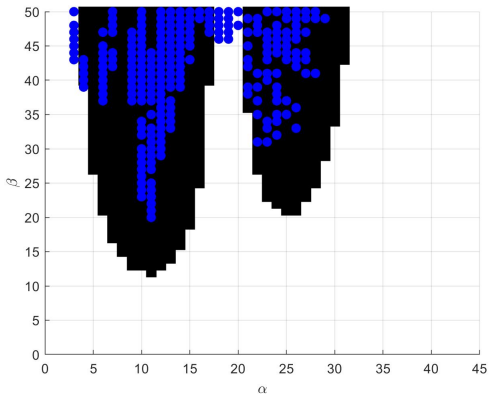

(b) Simulation results for Duffing chaos with horizontal displacement

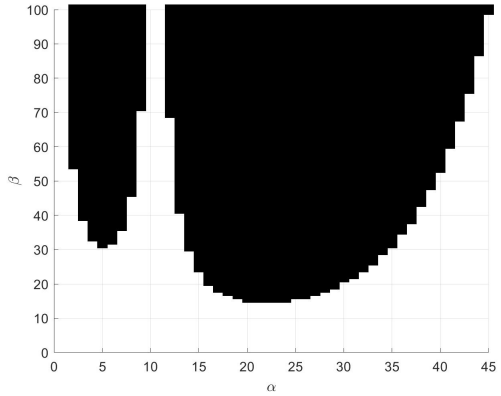

(c) Melnikov's results for Pendulum chaos with horizontal displacement

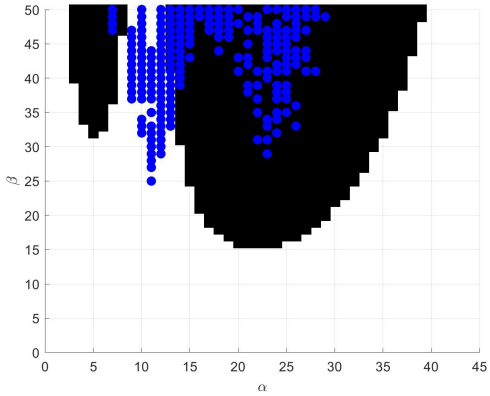

(d) Simulation results for Pendulum chaos with horizontal displacement

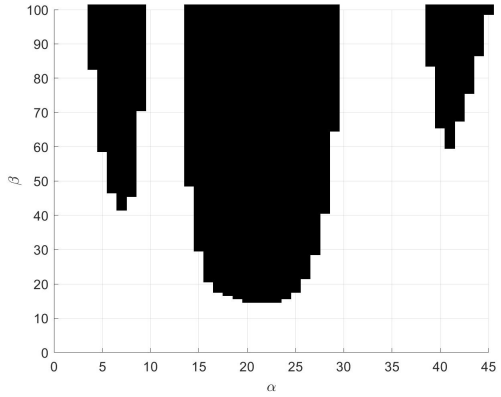

(e) Melnikov's results for both types of chaos with horizontal displacement

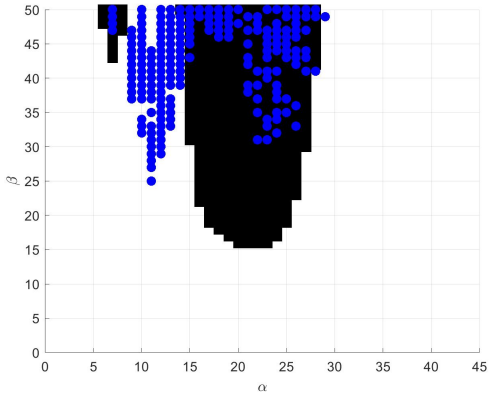

(f) Simulation results for both types of chaos with horizontal displacement

Figure 4.21: Simulation Results for parameters showing equal amounts of both Duffing and Pendulum Type chaos

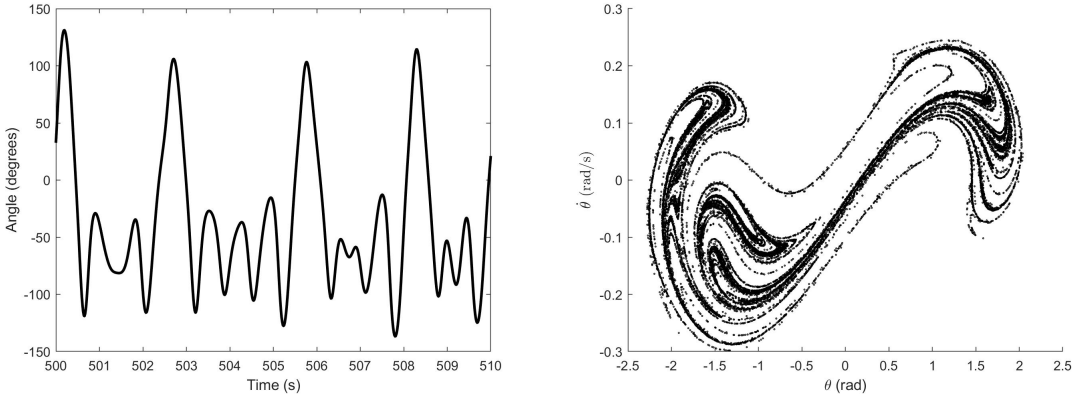

(a) Zoomed in time history (b) Poincaré Map

Figure 4.22: Simulation Results for sinusoidal parameters showing Duffing Type chaos with horizontal offset

Chapter 5

Discussion

5.1 Comparison of Melnikov's Method and Simulation Results

The results from Melnikov's method were used as a prediction of the onset of chaos for the WPP. The development of the simulation provided an easy way to check this method for the non-conservative system, as well as to gain a better understanding on the effect of sinusoidal forcing on the system. Overall, Melnikov's method is shown to be a valid tool in understanding the system's chaos, but is not able to accurately determine a "lower bound" of the chaotic regions. Melnikov's method did, however, accurately recreate the shapes of the chaotic regions, in the vicinity of these regions. These deviations from the simulation results are most likely a result of the analysis of the homoclinic orbits. The orbits used in the analysis were gathered from simulation data, which had damping present to reflect that of the physical system. As discussed earlier, Melnikov's method is only proven to be valid for the conservative system. As seen in Figure 2.9, damping has a significant effect on the orbits compared to the conservative system, and integrating about these orbits will skew the results.

Another consequence of Melnikov's method is that it views the two types of chaos as independent sets. This results in the predicted overlapping regions between the two types of

chaos, but this method can not predict how the system will act. The simulations, however, show the chaos types as regions that can merge and interact with each other. As can be seen in Figures 4.14 through 4.16, simulations at parameter values that are "deeper" into a chaotic region can display more of that type of chaotic behavior in the system dynamics. In fact, the two portions of the Poincaré map merge together and appear as a single image, as in Figures 4.17 and 4.18.

5.2 Parameter Space

The effect of the sinusoidal parameters on the dynamics of the system can be investigated through the simulation results. Changes in α and β affect the system in different ways. Increasing β tends to increase the energy of the chaotic activity. However, if two simulations only have a slightly differing β value, the systems normally have a similar dynamic response, and similar Poincaré maps. Increasing β sharply can bring more Pendulum Type chaos into the system, since this increases the energy in the system, and this chaos requires more energy in order to swing in full revolutions. When both types of chaotic motion are present, continuing to increase β eventually causes the Pendulum Type chaos to mask the Duffing Type chaos. Most regions in parameter space in which Pendulum Type chaos is present also show signs of Duffing Type chaos, so in order to see purely Pendulum Type chaos, large β values must be used.

In the non-chaotic regions of the parameter space, β still has an effect on the system dynamics. With very low values of β, the pendulum oscillates with a very small amplitude about the equilibrium point. As β increases, so does the amplitude of oscillations. However, these oscillations are not always uniform, as seen in Figure 4.7.

On the other hand, small changes in α can have large effects on the system's dynamic

response. While the chaotic regions in the parameter space appear to extend to $\beta \to \infty$, they only extend to finite α values, meaning specific ranges of alpha values are required for chaotic motion. With values too small, the dynamics of the system are able to overcome the sinusoidal forcing, and values too large can not produce a large enough excitation.

In fact, the chaotic regions appear to form into "clusters," or bands of α values, leading to separate regions of chaotic motion with either low or high α values. Small changes such as decreasing the damping, or small changes in the integration of the homoclinic orbits, can increase the number of these clusters beyond two. Since there are several points within the chaotic regions that did not display chaotic motion, it is possible that there are many of these clusters that can not be seen without a higher resolution of the parameter space, that make up the larger chaotic region. This could be investigated by testing the parameter space with a smaller step size of α and β.

5.3 Horizontal Displacement

The addition of the horizontal offset did have an impact on the onset of chaotic motion of the WPP. A surprising result was that there were very few simulations showing signs of just Duffing Type chaos. If there was chaotic motion, typically both types of chaos were observed. This also leads to the fact that Pendulum Type chaos was much more common with the horizontal offset, especially at lower α values. This could be due to the fact that with a large offset, the pendulum travels at a faster linear speed, adding energy to the system. When $\delta = 0$, there was a large chaotic region of Duffing Type chaos centered at $\alpha = 9$, however when $\delta = -.12$, this region requires higher values of β to be chaotic. On the other hand, the chaotic region with higher values of α occupies approximately the same area of parameter space. This reveals that the horizontal offset mostly affected chaotic motion

at lower sinusoidal frequencies, but not as much at higher sinusoidal frequencies.

Additionally, the chaotic regions are shifted to slightly higher α values, showing that slightly higher frequencies are required for chaotic motion. This was not predicted by Melnikov's method. This shifting could be due to a change in the moment of inertia of the system, as a horizontal offset of 30 millimeters does result in a significant change in I_z.

With the horizontal offset, the chaotic regions are not as well defined as with $\delta = 0$. When $\delta = 0$, for the most part every point within the area of the chaotic region, displayed chaos. However with $\delta = -.12$, the region is made up of spots of individual simulations that might or might not display chaotic motion (shown in Plot (b) of Figure 4.21). Due to the damping of the homoclinic orbit, Melnikov's method could not be expected to accurately identify these spots. It is possible that these spots are a result of the region being formed by smaller clusters, as described in the previous section. Alternatively, the edges of chaotic regions are often fractal in nature, so these spots could also be due to a lack of a clear boundary. Investigating this would require an undamped homoclinic orbit to integrate about, which is explained further in the following section.

5.4 Accuracy of the Results

As mentioned in Section 5.1, the results from Melnikov's method did not accurately derive a lower bound for the onset of chaos, but they did approximate the locations of the chaotic regions. However, these regions were predicted to have a sinusoidal frequency of a couple radians/sec different than the simulations usually showed. These differences most likely come from the damping of the homoclinic orbits used for the integrals in Melnikov's method. Even if a undamped homoclinic orbit was used in order to correspond better with the Melnikov's method results for a conservative system, the inclusion of damping in the simulation will

still cause contrasting results.

In general, for $\delta = 0$, Duffing type chaos was prevalent at both lower ($\alpha < 10$) and higher ($\alpha > 15$) values of α. Pendulum Type chaos was prevalent at higher values of alpha. Melnikov's method identified the chaotic regions fairly well: it successfully identified the minimum of the lower α region, but was slightly shifted horizontally (along the α axis). The higher α region was also predicted accurately by Melnikov's method, but also predicted lower values of β to be capable of producing chaotic motion than the simulation showed. These higher frequencies were most likely dampened in the simulations, and were unable to produce chaos until greater amplitudes were used.

Another source of error occurred in the area between the lower and higher α regions. This area was predicted to have no chaotic motion, while the simulations showed it to have both types of chaos for higher values of β ($\beta > 40$). This again could be due to damping in the homoclinic orbit used, however, it could also have an explanation in the dynamics of the system. Melnikov's method treats the types of chaos as independent sets, while in reality their interactions might cause additional chaos. On the borders of chaotic regions, small deviations along one orbit might cause enough excitations along the other homoclinic path to create intersections of the unstable and stable manifolds. This behavior would not be predicted when investigating just one orbit at a time.

5.5 Experimental Testing

The use of the physical system helped to verify the mathematical modeling of the local bifurcations of the system. The pendulum's behavior corresponded well with the numerical computations of the cusp and equilibrium paths. The physical system also proved to be helpful in verifying the simulation data towards the global bifurcations and chaotic motion.

Although the experiments could not be run for long enough to develop a complete Poincaré map, they were still able to show evidence of a strange attractor, verifying the analysis of the simulations. However, jitter in the control input caused the sinusoidal frequency to slightly vary among the time periods. This causes problems in developing the Poincaré map, as the time period is no longer constant. This could cause distortion of the image of the strange attractor, depending on the severity of the jitter. However, this does not prevent the experiment from showing evidence of chaos, as the general shape of the strange attractor remains intact.

Care must be taken when gathering experimental data using the physical system. A lot of interesting dynamics are experienced with the use of extreme parameters, such as large values of ω and Δ, but these situations also prove very stressful on the system. This is why the development of the simulation to work alongside the experimental system is very valuable.

5.6 Future Research

In order to expand on the topics discussed in this thesis, future research can be done using the Whirling Planar Pendulum system. In particular, it would be interesting to investigate the location of the chaotic regions in the (α,β) parameter space. This could help to understand why there is no chaotic motion when the system is excited with moderate frequency values (α values).

Additionally, some parameters (such as the geometry of the pendulum) may affect the shape of the chaotic regions in the parameter space, which can be done in order to maximize or minimize the α and β values needed to create chaotic motion. An analysis of these could be useful in applications where chaos is detrimental to the dynamic system.

Chapter 6

Summary

The results detailed in this report illustrates the occurrence of the local and global bifurcations of the Whirling Planar Pendulum. To add onto the previous mathematical modeling of the system, the full equilibrium manifold of the dynamic system was modeled using experimental data gathered from a physical WPP system, and operated from a Simulink model. This system includes a controllable horizontal offset, which allows for the investigation into the perturbation of the local pitchfork bifurcation, and leads to a cusp which bounds the parameter space in which there are multiple stable equilibrium values. This system, as well as a simulation of the WPP, was used to investigate the occurrence of chaotic motion when excited with a time-varying, sinusoidal input spin rate. This lead to an analysis to determine the parameter regions in which chaos could be predicted. Melnikov's method was used to determine the onset of two independent types of chaotic motion, termed "Duffing Type" chaos and "Pendulum Type" chaos. Using both simulations and results from the experimental setup, it was shown that the WPP system can experience both types of chaos simultaneously at certain points in the parameter space.

Bibliography

[1] M. Golubitsky and D. G. Schaeffer. *Singularities and Groups in Bifurcation Theory*. Springer-Verlag, New York, 1985.

[2] J. Guckenheimer and P. Holmes. *Nonlinear Oscillations, Dynamical Systems, and Bifurcations of Vector Fields*. Springer-Verlag, New York, 1983.

[3] G. Lajoie. The hartman-grobman theorem and the equivalence of linear systems. pages 1–14, 05 2019.

[4] J. E. Marsden and T. S. Ratiu. *Introduction to Mechanics and Symmetry*. Springer-Verlag, New York, 1994.

[5] F. C. Moon. Fractal boundary for chaos in a two-state mechanical oscillator. *Phys. Rev. Lett.*, 53:962–964, 1984.

[6] F. C. Moon, J. Cusumano, and P. J. Holmes. Evidence for homoclinic orbits as a precursor to chaos in a magnetic pendulum. *Physica D*, 24:383–390, 1987.

[7] S. W. Shaw and S. Wiggins. Chaotic dynamics of a whirling pendulum. *Physica D*, 31:190–211, 1988.